STUDY OF LOW ENERGY POSITRON-HELIUM SCATTERING

--PRECISE MEASUREMENTS OF TOTAL CROSS SECTIONS FROM 0.6 TO 22 eV--

TATSUMI MIZOGAWA

1984

STUDY OF LOW ENERGY POSITRON-HELIUM SCATTERING
-- PRECISE MEASUREMENTS OF TOTAL CROSS SECTIONS FROM 0.6 TO 22 eV --

A Thesis Presented

by

TATSUMI MIZOGAWA

to

The Faculty of Engineering
in partial fulfillment of the requirements
for the degree of Doctor of Engineering

KYOTO UNIVERSITY
KYOTO, JAPAN
October 1984

ACKNOWLEDGMENTS

The present thesis has been submitted to the Department of Nuclear Engineering of Kyoto University in partial fulfillment of the requirements for the degree of Doctor of Engineering. This study has been performed in the Laboratory of Nuclear Radiation, the Institute for Chemical Research of Kyoto university, from April 1977 to July 1984.

The author wishes to acknowledge sincerely to Dr. Yasuyuki Nakayama for his continuous encouragement and exhaustive discussions through all phases of this work.

Dr. Rintaro Katano is gratefully acknowledged for his many invaluable suggestions on the design of the present experimental apparatus. The author greatly appreciates the valuable assistance of Messrs. Tatsumi Kawaratani and Mitsuo Tosaki throughout the long duration of this work. He is also grateful to Drs. Yasuhito Isozumi and Shin Ito for their valuable help in the data analysis, and for their stimulating discussions. Furthermore, he is indebted to Associate Professor Hiromasa Mazaki and Dr. Takeshi Mukoyama for their useful advices.

Finally, the author would like to express his sincere gratitude to his parents, for their understandings and continuous encouragements.

CONTENTS

ABSTRACT

Precise measurements for positron-helium absolute total cross sections (TCS's) have been performed over the energy range from 0.6 to 22 eV with a high resolution time-of-flight spectrometer.

Since the Ramsauer effect occurs around 2 eV, discrimination against forward scattering is of special importance for precise determination of the TCS's. The spectrometer, characterized by a straight flight tube and weak axial magnetic field, has been designed to achieve effective reduction of the errors due to forward scattering.

The results around the Ramsauer minimum are close to the theoretical results by Campeanu and Humberston, and remaining slight discrepancies are fully explained by taking account of imcomplete discrimination against forward scattering. In the energy region excluding the vicinity of the minimum, the overall error is a few percents. Above $\sim$5 eV, an excellent agreement between our results and some theoretical works has been found. Above 17.8 eV (the positronium-formation threshold), our results reasonably agree with other experimental TCS's.

CHAPTER I

INTRODUCTION

Experiments on positron-atom collisions with monoenergetic slow-positron beam are interesting from many points of view. First, a positron colliding with an atom can be regarded simply as a "positive-charge electron" in non-relativistic energy region, because the annihilation probability during the collision is quite small. Consequently positron-atom collisions are complementary to electron-atom collisions for testing approximation methods of the collision theories. Second, if a precise wave function of a colliding positron-atom system is revealed through collision experiments, the wave function can be used for calculating a direct annihilation cross section, which provides fundamental information for the study of positron life-time spectra in gases. Finally, there exists an electron pick-off channel, i.e. the positronium (Ps) formation channel. The data of Ps-formation cross sections provide another basic information for the interpretation of the lifetime spectra in gases. In addition, the Ps-formation may become a predominant route which leads positrons to annihilation in rarefied and hot gases, and the data of the cross sections may possibly play an important role in astrophysics[1] or other fields.

Since a monoenergetic slow positron beam was first put into practical use by Costello et al.,[2] many experimental efforts have been devoted to the study of low-energy positron-atom collisions.[3]

Most part of the efforts has been concentrated on the measurements of the total cross sections (TCS's). One of the reasons is that the TCS's can be measured with comparative ease and higher accuracy than the other quantities. The other reason is that they have practical importance providing the standard for other quantities obtained in "relative" measurements (for example, recent "direct" measurements of the Ps-formation cross sections,[4,5] differential cross sections,[6] and inelastic cross sections[7]). At the present stage, there exixt many results of the TCS's for a large variety of target atoms. Generally speaking, the agreement among the works of different groups is still unsatisfactory, although the situation is improving year after year.[3]

Above all, positron-helium TCS's are of special importance. Experimentally, positron-helium is the simplest system to be handled with a practicable manner. Theoretically, it is also the simplest case next to the positron-hydrogen system, on which the calculation of scattering parameters can be performed with no baseless approximation to simplify the first principle (the Schrödinger equation). Thus the case provides a unique stage

today where reliable theoretical results and precise experimental data can possibly be compared. Once the consistency between both results are established, the results will give a firm standard to examine the validity of simpler approximate theories and experimental methods which are applicable to more complex systems.

Previous experimental data[8-12] of the positron-helium TCS's are now in general agreement over the major part of measured energy range. The characteristic features of TCS vs energy curve (which are common to most of target gases) are the existence of the Ramsauer-type minimum at a few eV and the discontinuous change of the slope at the Ps-formation threshold.

Quantitatively, however, appreciable ambiguity in the experimental positron-helium TCS's still exist, e.g., in the energy region around the Ramsauer minimum. The TCS's by Stein et al.,[8] which are the first direct observation of the Ramsauer effect in positron-atom collisions, are about 20% lower than those of Canter et al.[9] around the minimum. The results of Burciaga et al.[10] are further lower than those of Stein et al. in this region. The recent results of Wilson[11] (corrected by Sinapius et al.[12]) are close to those of Canter et al. The purpose of this study is to resolve such ambiguity and to give more reliable experimental TCS's of positron-helium collisions.

Theoretical calculations of phaseshifts for positron-helium collisions have been reported by a number of authors. They show qualitatively similar shape of the TCS curve including the Ramsauer-type minimum. For *s*- and *p*-wave, elaborate calculations by the Kohn variational method were performed,[13-16] and the results provide the most reliable *s*- and *p*-wave phaseshifts at present. The theoretical TCS's deduced from the two and higher partial-wave phaseshifts by the effective-range theory of O'Malley et al.[17] are in relatively better agreement with the experimental TCS's than other combinations of phaseshifts. Near the Ramsauer minimum, this theoretical results seem to support the TCS's of Wilson or Canter et al.

The ambiguity, however, should be resolved by new experiments with taking measures for possible systematic error sources. Humberston[18] pointed out the possible underestimate of the TCS's in the works of Stein et al. and Burciaga et al. due to insufficient discrimination of forward-scattered positrons, which, in the transmission methods, should be removed from incident beam for exact determination of the TCS's. In accordance with this suggestion, Wadehra et al.[19] examined the results of Stein et al. and found that the discrimination angle (the maximum allowed scattering angle for positrons to stay in the beam) of 17° can explain the discrepancy between the theory and the

results of Stein et al. Meanwhile the discrimination angle of Wilson's apparatus was reported to be 5° (in later work, more conservative estimate 7° was reported[12]), which means that their apparatus is fairly free from the forward scattering error. Their results are in reasonable agreement with the theory. Thus the discrepancy among the experimental TCS's can be interpreted consistently with the incomplete discrimination against forward scattering.

It is apparent that further measurements are still required. The measurements of Wilson cover rather narrow energy range (1-6 eV), and the resultant TCS's are deduced by a manner of normalization procedure. The results of Canter et al., which are also in good agreement with the theory near the Ramsauer minimum, did not extend below 2 eV, and failed to reveal the minimum of the TCS's directly.

In a new experiment, sufficient precaution for the minimization of the forward scattering error should be paid, and desirably, the variation of the observed TCS's with the reduction of the discrimination angle can be demonstrated by using the identical apparatus. The present spectrometer, based on a time-of-flight (TOF) technique, was designed on this line.

In CHAPTER II the present TOF spectrometer is described. Experimental procedure and methods of data analysis are described in CHAPTER III. Intensive discussion on the

present experimental errors is given in CHAPTER IV. Finally in CHAPTER V the results are presented, and compared to the other experimental and theoretical results. Conclusions are also presented there.

CHAPTER II

TIME-OF-FLIGHT SPECTROMETER

A. Principle and Outline

Schematic diagrams of a time-of-flight (TOF) spectrometer and details of the slow-positron source assembly are shown in Figs. 1 and 2, respectively.

A solenoid coil consisting of three sections was wound around the vacuum chamber so that it produces almost uniform axial magnetic field over the whole flight path. This results in the increase of transmission of slow positrons by guiding them along the axial field. Such a field has been often employed by previous experimental groups,[8-10] for it is inevitable to make the experiment practicable against the weakness of incident beam. It can cause, however, two kinds of systematic errors which become significant in a low energy region. One is the underestimate of total cross sections (TCS's) due to the incomplete discrimination against forward scattering and the other is the overestimate of the TCS's due to the increase of positron path-length in the gas cell by spiralling. It should be noted that both effects become small as the product of the field strength and the geometrically allowed spiralling radius becomes small. Therefore our actual choice is to minimize the product as far

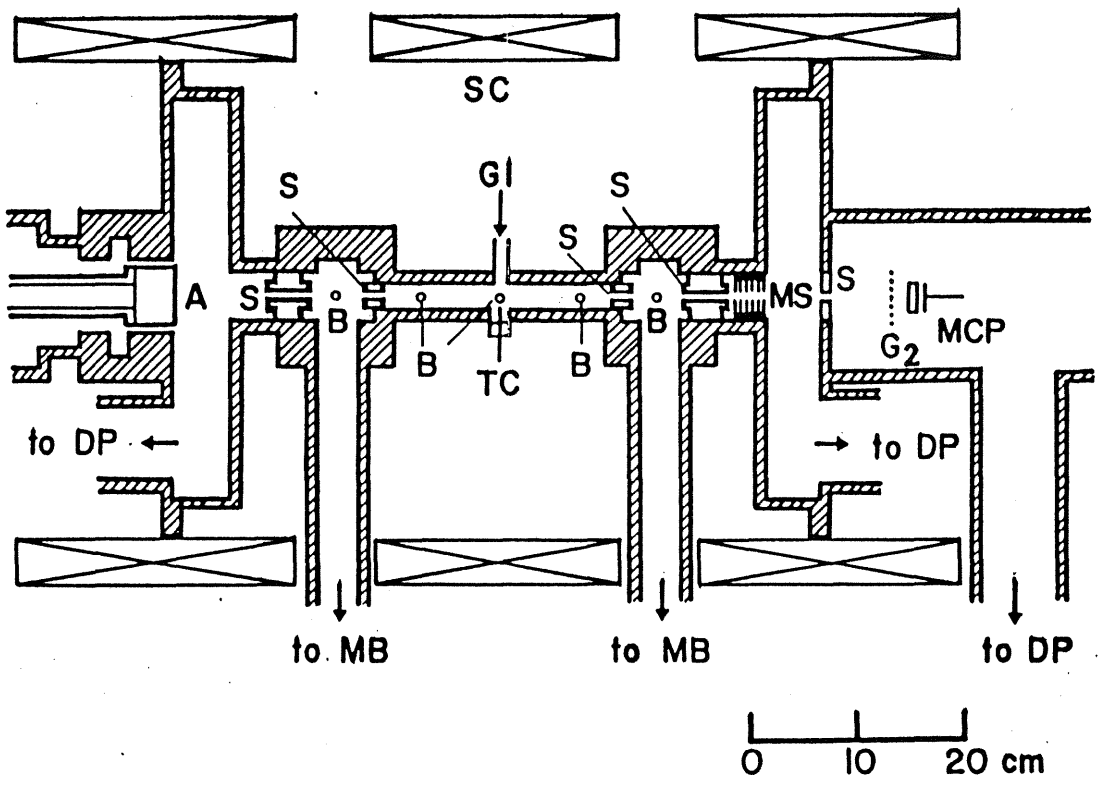

Fig. 1. Time-of-flight spectrometer. A, source-moderator assembly; S, 4-mm-diameter cylindrical apertures; B, pressure-gauge ports (for Baratron 310BHS); TC, thermo-couple; GI, gas inlet; MS, multi-slit; MCP, micro-channel-plate detector; DP, oil diffusion pump with water-cooled baffle; MB, mechanical booster pump with liquid-nitrogen-cooled trap; SC, solenoid coil consisting of three sections; G_2, grounded grid.

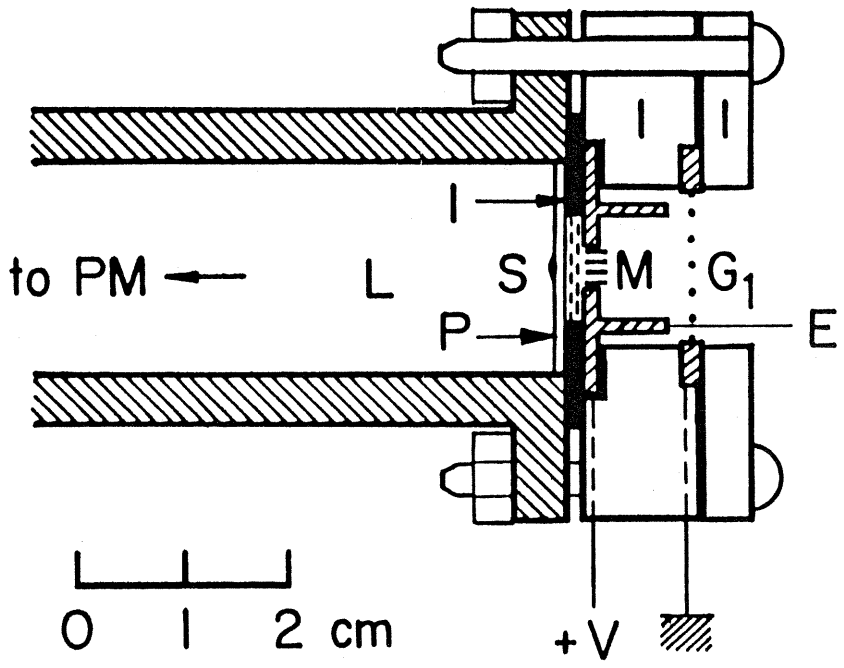

Fig. 2. Details of source-moderator assembly. L, light pipe; S, ^{22}Na source; P, plastic scintillator; M, tungsten moderator; G_1, grounded grid; E, accelerating electrode; I, insulators; PM, photomultiplier.

as the loss of incident beam is tolerable. The present spectrometer was constructed after this consideration, and is characterized by a straight flight tube, a localized gas cell, weak magnetic field, and a small-radius cylindrical aperture system which confines paths of incident and scattered positrons close to the spectrometer axis. Furthermore, the uniformity of the magnetic field makes quantitative evaluation of the errors mentioned above quite simple, as discussed in CHAPTER IV.

About 90 μCi of ^{22}Na was mounted between a light-pipe and a plastic-scintillator disk (2-cm diameter and 0.4-mm thickness). The scintillator provides one timing signal for the TOF measurements when a fast positron from the source penetrates the scintillator. The fast positron then impinges on a moderator consisting of tungsten ribbons and meshes. A slow positron, re-emitted from the moderator and accelerated to a desired energy, is transported through five 4-mm-diameter cylindrical apertures along the axis of the straight flight tube, and finally detected by a micro-channel-plate detector (MCP) which provides the other timing signal. The distance between the moderator and the first grounded grid G_1 is 1 cm, and that between G_1 and the second grounded grid G_2 in front of the MCP is 66 cm. Kinetic energy of a positron is determined from these lengths and the measured flight time.

Tareget gas is introduced into the gas cell at the cell center via a double molecular-sieve trap cooled by liquid-nitrogen. The flowing gas is pumped out from both sides of the gas cell by a mechanical booster pump with a liquid-nitrogen cooled trap. The TCS's can be determined from the ratios of slow positron counts in the same energy bin of a pair of TOF spectra, one with gas and the other without gas.

Detailed description of each section of the present TOF spectrometer is given below.

B. Source-Moderator Assembly

1. Preparation of a ^{22}Na source

Source preparation is depicted in Fig. 3. Commercially available carrier-free ^{22}Na of $\sim$100 μCi (sodium chloride in aqueous solution) was diluted with about 0.1 normal hydrochloric acid, and the solution was condensed by heating to about 3 $\mu\ell$. Subsequently, it was carefully dripped at the center of the scintillator disk so as to form a spot of less than 2-mm diameter, and dried up. The spot was covered with a thin film of rubber hydrochloride (RHC), and the disk was set on a photomultiplier light pipe (made of Lucite) by the use of Dow Corning 20-057 optical coupling compound, with source-side inbetween.

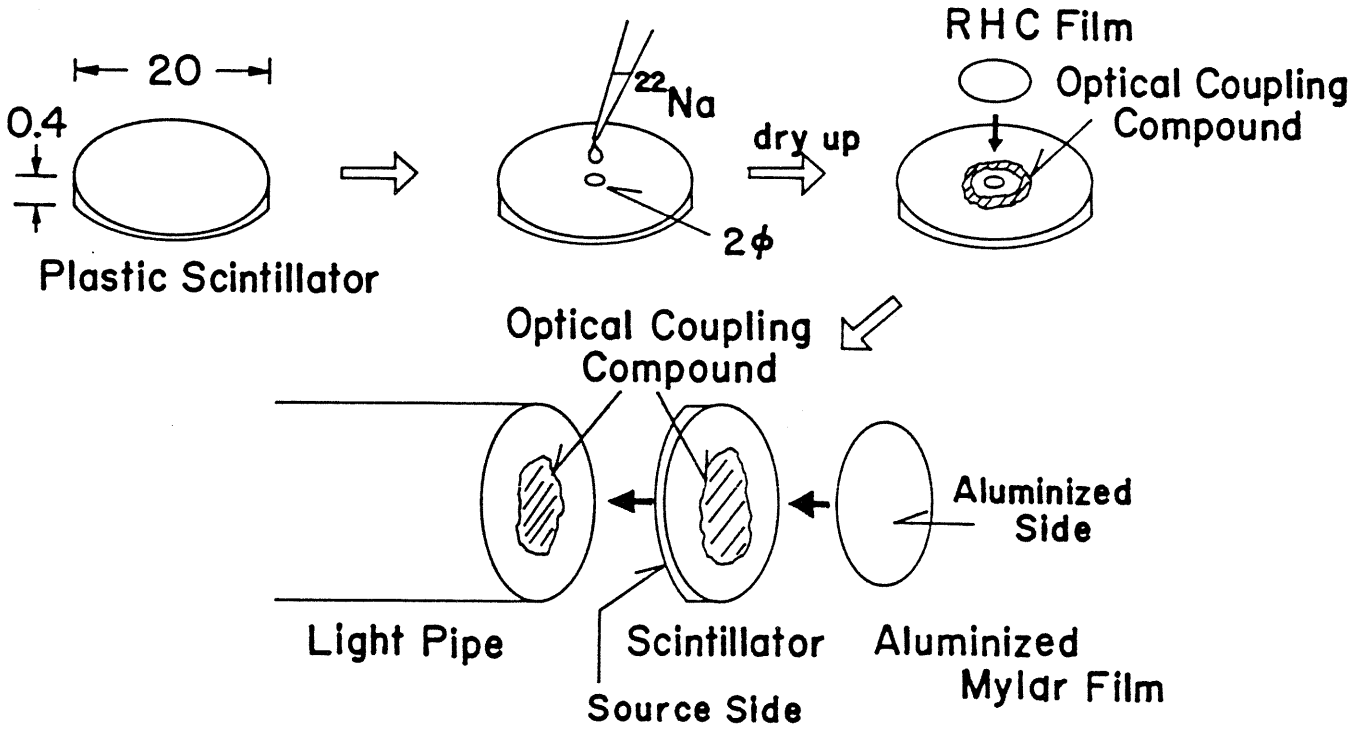

Fig. 3. Preparation of ^{22}Na source.

Numerical values are in mm.

2. Moderator preparation

The present moderator consists of tungsten ribbons (0.025-mm thick and ∿2-mm wide) and meshes (0.02-mm wire diameter and 100 meshes per inch), and was prepared according to a similar manner to Dale et al.[20] Both ribbons and meshes were swabbed with acetone, and rinsed first by acetone and next by ethanol in a ultrasonic cleaner. They were then electropolished in 2.5-normal NaOH, and rinsed once more by ethanol. Subsequently, they were heated to ∿2200 °C in 6 x 10^{-7} Torr by passing electrical current. After ∿5-minute heating and turning off the current, they were cooled down to room temperature naturally in vacuum.

3. Installation of source-moderator assembly

As shown in Fig. 2, the ^{22}Na source and the moderator were mounted, and then installed in the spectrometer. Four sheets of tungsten ribbons (∿4-mm long) were aligned with their surfaces parallel to the spectrometer axis and with ∿1-mm distance, and were fixed to an accelerating electrode made of copper (or brass) with electroconductive resin. Several sheets of tungsten mesh (∿1 cm x 1 cm) were sandwiched between the scintillator disk and the accelerating electrode. Both ribbons and meshes serve as moderators. The moderator side of the scintillator disk was covered with aluminized Mylar, of which aluminized surface was electrically contacted with the moderator. Slow positrons re-emitted from the

moderator surface are accelerated to a desired energy by electrical field applied between the moderator and the subsequent grounded grid G_1 (tungsten, 0.03-mm wire diameter and 30 meshes per inch). All parts were fixed by Teflon insulators to a flange of an aluminium cylinder supporting the light pipe.

C. Detection System and Electronics

1. Plastic scintillator

A 0.4-mm-thick and 2-cm-diameter disk of NE104 fast plastic scintillator was used for detecting the emission of fast positrons from the ^{22}Na source. A light flashing of the scintillator due to the energy loss of a fast positron is detected via the light pipe by an RCA 8575 photomultiplier tube.

2. Micro-channel-plate detector

At the end of flight path, slow positrons are detected by a Galileo 3025 chevron micro-channel-plate detector (MCP) of which active diameter is 20 mm (see Fig. 4). A slow positron passed a grounded grid G_2 is accelerated by a voltage applied to the grid G_3 (-200 V) and detected by the MCP. Both G_2 and G_3 are made of tungsten mesh same as G_1. The anode of the MCP was divided to two concentric parts. As the diameter of slow positron beam is $\sim$4 mm, the MCP signals were taken only

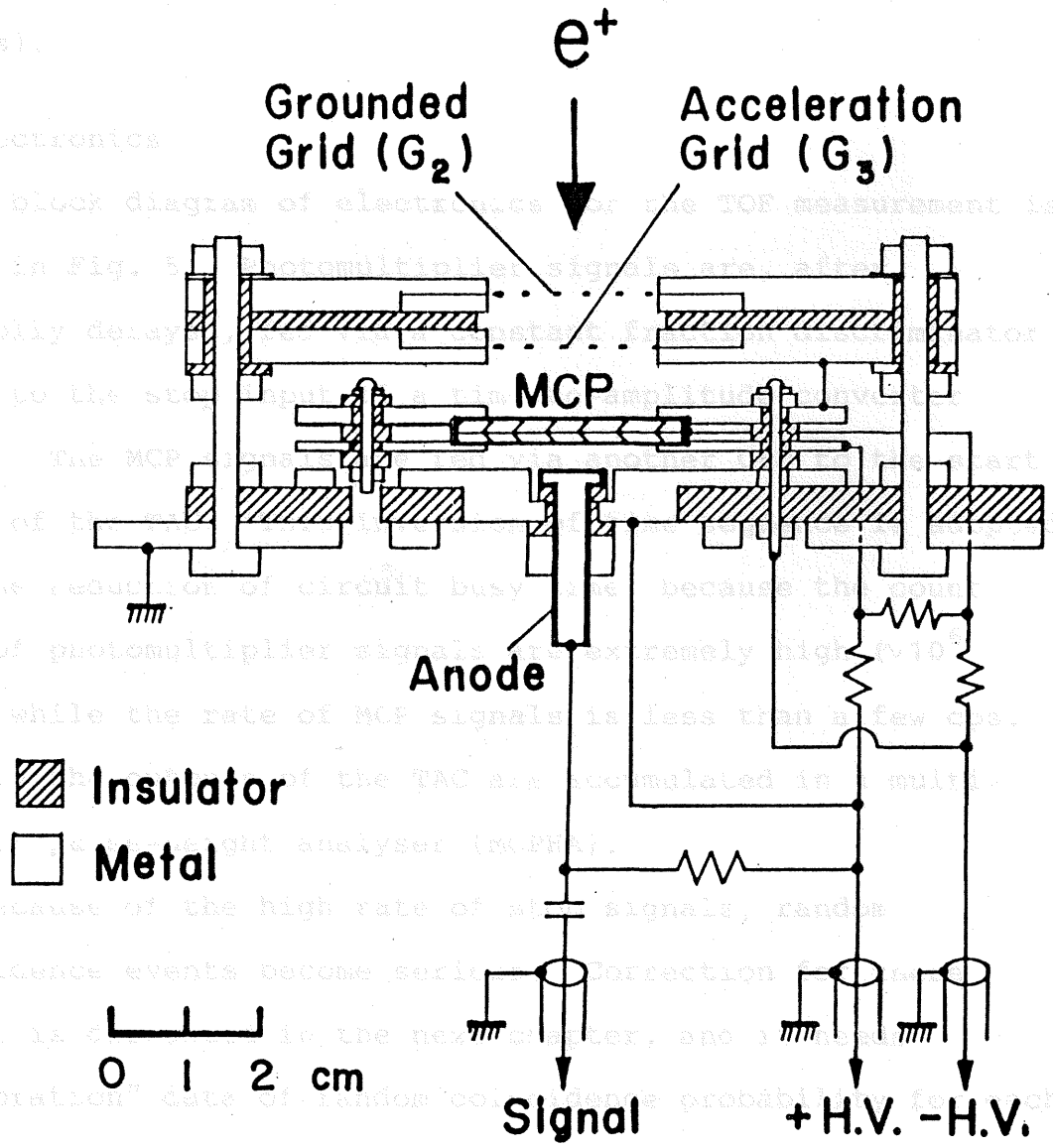

Fig. 4. Mounting of micro-channel-plate detector.

from the inner anode (8-mm diameter). The outer anode may detect only background events (e.g., positive ions and dark counts).

3. Electronics

A block diagram of electronics for the TOF measurement is shown in Fig. 5. Photomultiplier signals are, after suitablly delayed, fed via a constant fraction discriminator (CFD) to the stop input of a time-to-amplitude converter (TAC). The MCP signals are fed via another CFD to the start input of the TAC. This inversion of time sequence is adopted for the reduction of circuit busy time, because the count rate of photomultiplier signals are extremely high ($\sim 10^6$ cps), while the rate of MCP signals is less than a few cps. Finally the outputs of the TAC are accumulated in a multi-channel pulse-height analyser (MCPHA).

Because of the high rate of stop signals, random coincidence events become serious. Correction for these events is discussed in the next chapter, and it needs "calibration" data of random coincidence probability for each TOF channel. The "calibration" spectra are measured by replacing MCP signals with 60-Hz regular pulses.

4. Time resolution of detection system

Overall time resolution of the detection system was measured by observing the prompt peak due to γ ray and/or

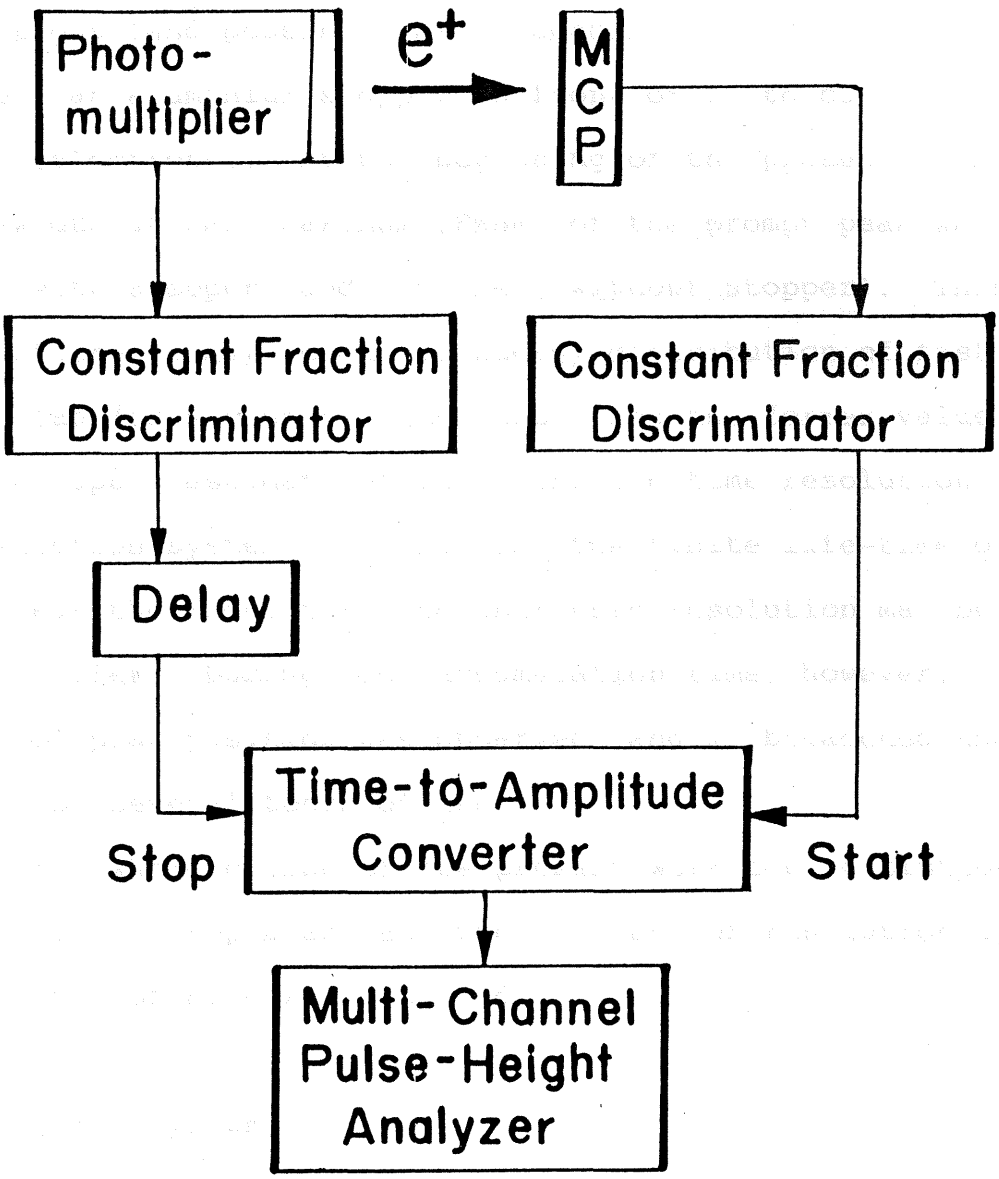

Fig. 5. Block diagram of electronics for time-of-flight measurement.

fast positrons (and possibly fast secondary electrons), with and without an aluminium stopper in front of G_1 to cut positrons (electrons). At the beginning of the present work, the full-width at half-maximum (FWHM) of the prompt peak was 1.2 nsec (with stopper) and 1.6 nsec (without stopper). This obvious difference may be due to energy distribution of fast positrons (and/or secondary electrons), and the former value may give an upper estimate of the intrinsic time resolution of the detection system. Considering the finite life-time of positron near the moderator, the intrinsic resolution may be slightly smaller. During long accumulation time, however, the drift of peak position was observed, and it broadened the peak width by several tenth of nsec.

After the whole course of the present work the resolution measurements were repeated, and the decrease of resolution by several tenths of nsec was observed.

D. Gas Handling System

Schematic diagram of the gas handling system is given in Fig. 6. Target gas of 99.999% or 99.9999% purity is introduced at the center of the gas cell via a precision needle valve, a liquid-nitrogen-cooled molecular-shieve trap, a piezoelectric valve, and second molecular-shieve trap. During the introduction, the "bypass" valve is closed and

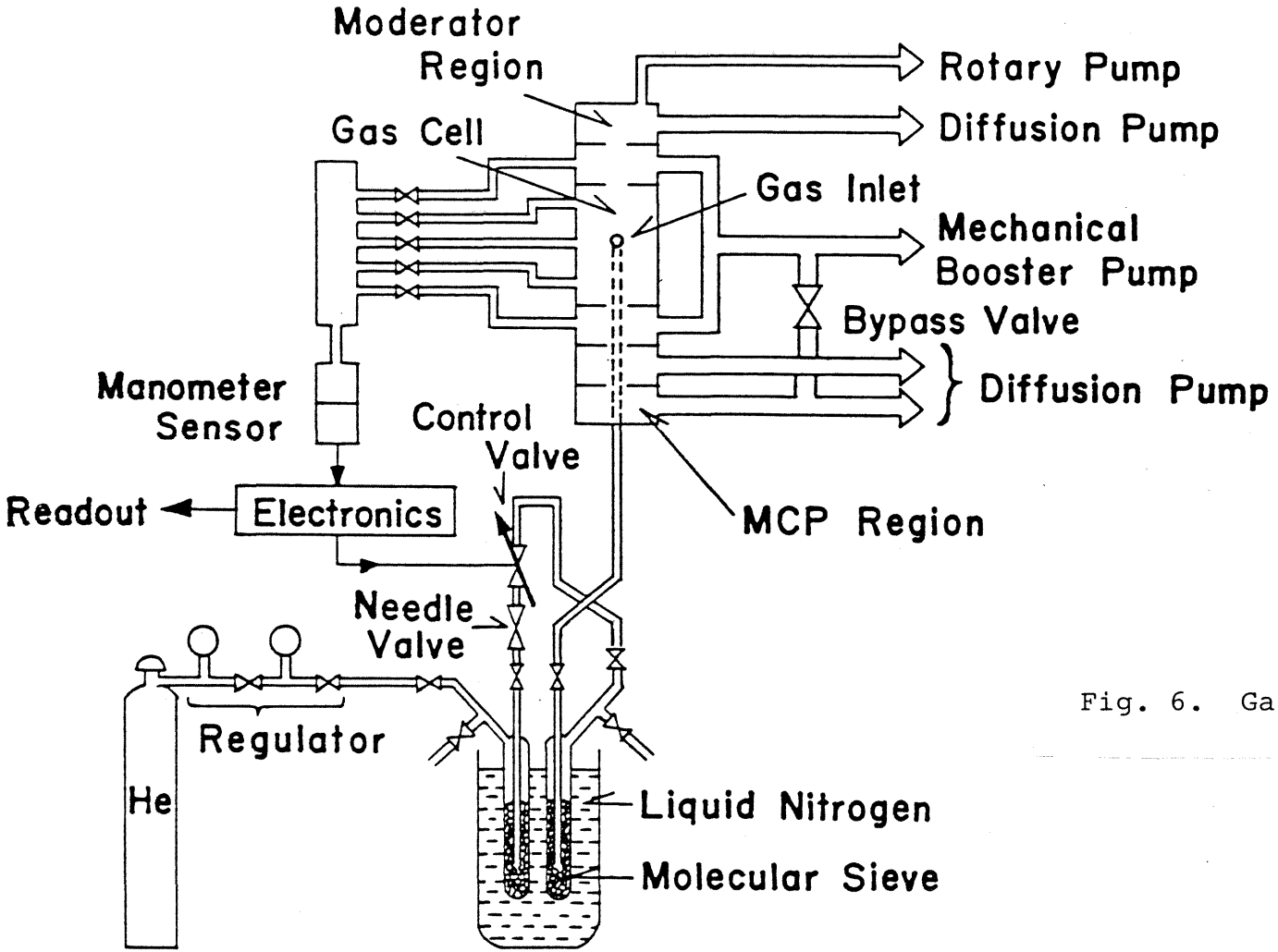

Fig. 6. Gas handling system.

both sides of the gas cell are pumped by a mechanical-booster pump (MB) with liquid-nitrogen-cooled trap. When the gas is not supplied, the "bypass" valve is opened and both sides of the gas cell is evacuated by an oil-diffusion pump with water-cooled baffle. Pressure can be measured by a precision capacitance manometer (Baratron 310BHS) at five ports, and by three ionization gauges. Gas flow is automatically controlled to keep the pressure constant by the piezoelectric valve.

The pressure distribution in the flight tube was measured by controlling the gas flow manually with the needle valve. The pressure in the regions neighboring the gas cell (P_2) relative to that of the gas cell (P_1) increases from 1/7 to 1/6 with the decrease of P_1 from 0.12 to 0.04 Torr (see Fig. 7), due to the decrease of pumping speed of the MB at the low pressure. P_2 is not negligible to evaluate the target thickness. Hence, during the measurement of the TCS's, the observed ratio P_2/P_1 was used for evaluation of P_2, because the manometer sensor was exclusively used to measure P_1 for the auto-control of gas flow. When the gas is not introduced, the pressures in the moderator region and the MCP region were less than 5×10^{-6} and 3×10^{-6} Torr respectively. The reading of the ionization gauge at the MCP region was not affected by the gas introduction, while that of the moderator region was increased by $\lesssim 5 \times 10^{-6}$ Torr. As

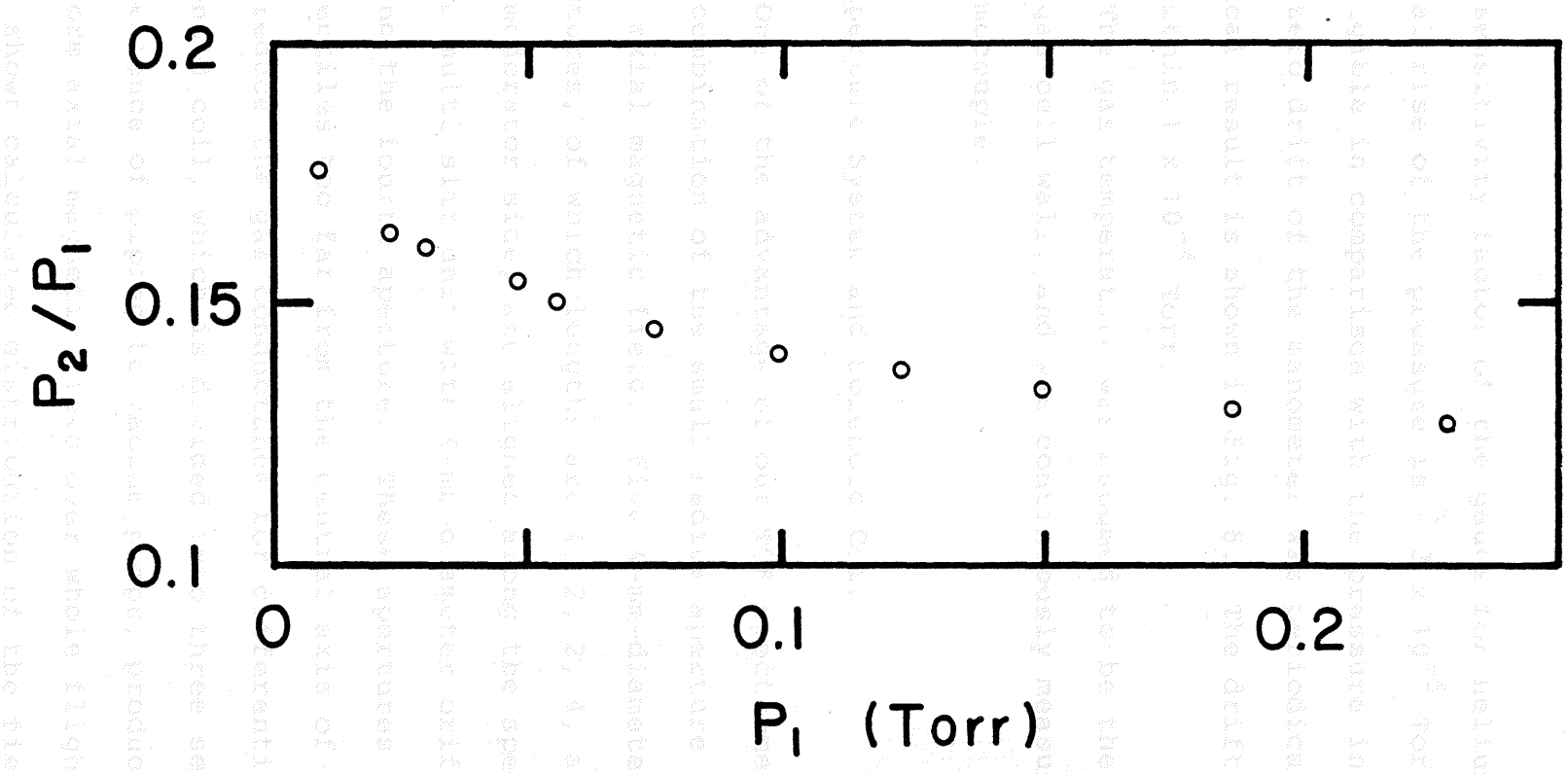

Fig. 7. Measured ratios of the pressures in the regions neighboring the gas cell (P_2) and that in the gas cell (P_1).

the sensitivity factor of the gauge for helium is 0.15, the actual rise of the pressure is $\lesssim 3 \times 10^{-5}$ Torr, which is negligible in comparison with the pressure in the gas cell.

Zero drift of the manometer was periodically checked. Typical result is shown in Fig. 8. The drift in several days is within 1×10^{-4} Torr.

The gas temperature was assumed to be the same as that of the gas-cell wall, and was continuously measured by a thermocouple.

E. Aperture System and Solenoid Coil

One of the advantage of our TOF spectrometer comes from the combination of the small radius aperture system and the weak axial magnetic field. Five 4-mm-diameter cylindrical apertures, of which lengths are 4, 2, 2, 4, and 1.6 cm from the moderator side, are aligned along the spectrometer axis, and a multi-slit unit with 4-mm-diameter orifices is located behind the fourth aperture. These apertures remove the projectiles too far from the central axis of the apertures, and reduce the gas conductance for differential pumping. A solenoid coil, which is divided into three sections for convenience of piping to vacuum pumps, produces approximately uniform axial magnetic field over whole flight path. In Fig. 9 is shown calculated distribution of the field strength with the locations of the moderator, the apertures, and the MCP.

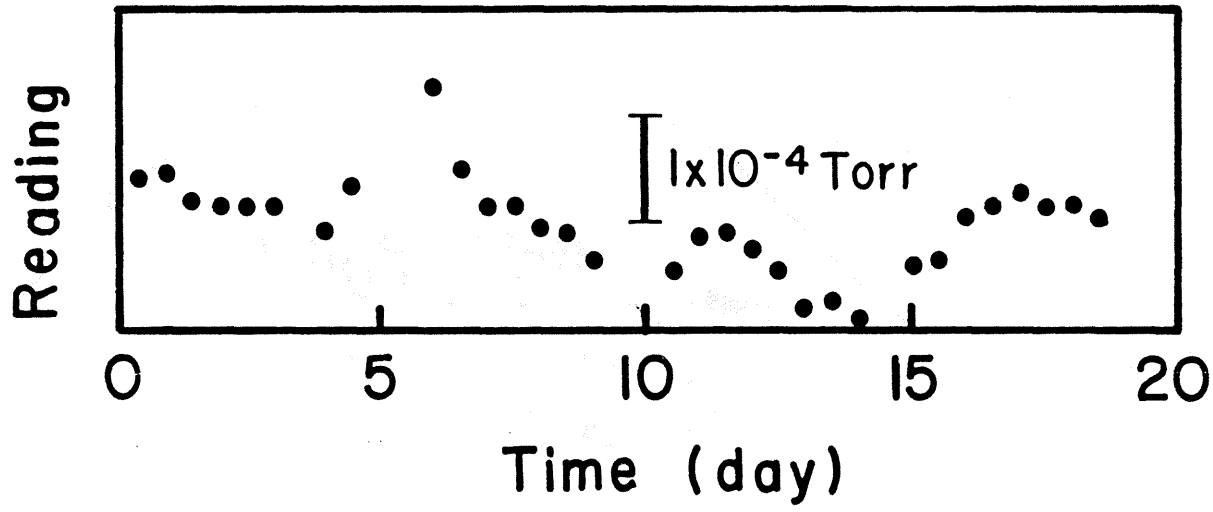

Fig. 8. Observed zero drift of capacitance manometer (Baratron 310BHS). Real pressure is less than 1×10^{-5} Torr.

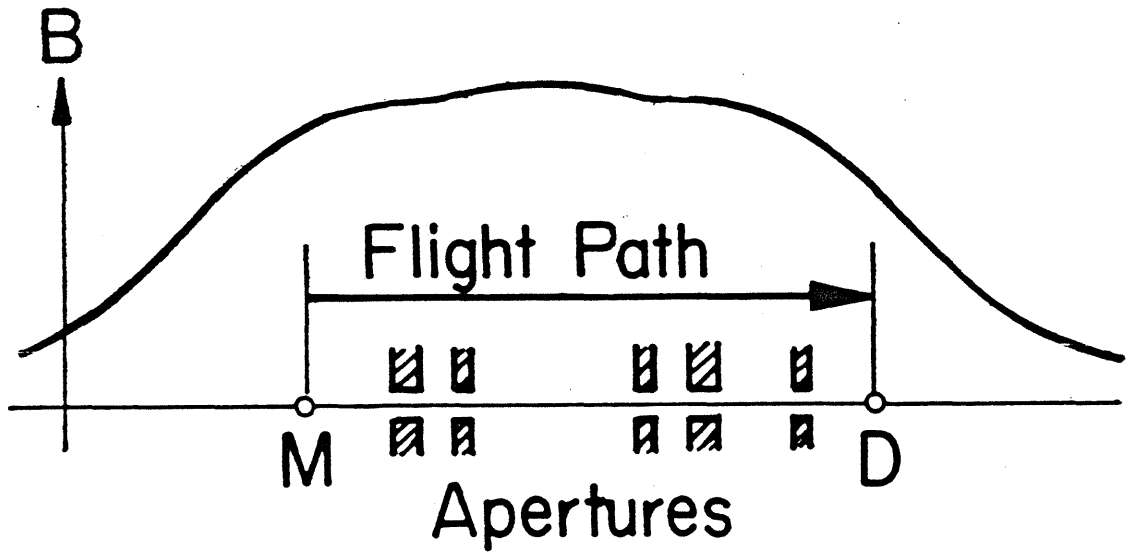

Fig. 9. Calculated axial magnetic field produced by solenoid coil consisting of three sections. M, moderator; D, micro-channel-plate detector.

In this axial field projectiles fly along the spectrometer axis with approximately constant spiralling radius over the whole flight path. In the magnetic flux density B, the spiralling radius r is given by

$$r = \frac{mv_2}{eB} \quad , \tag{1}$$

where v_2 is the component of velocity perpendicular to the field B, and m, e are the positron mass and charge. When the magnitude of r is confined by the aperture system to be less than R,

$$v_2 < \frac{eBR}{m} \quad . \tag{2}$$

Non-zero value of v_2 causes several kinds of systematic errors in TCS measurements. Equation (2) suggests a simple way adopted in the present work to minimize such errors, i.e. to reduce BR as far as the loss of beam intensity is tolerable. Besides, the geometrical simplicity of our spectrometer enables us to estimate such errors by a straightforward way, as will be discussed in CHAPTER IV.

Another reason for the requirement to minimize v_2 is that the effective energy resolution of the TOF spectrometer is restricted by the distribution of v_2 (see below).

As shown in Fig. 10, the yields of slow positrons and

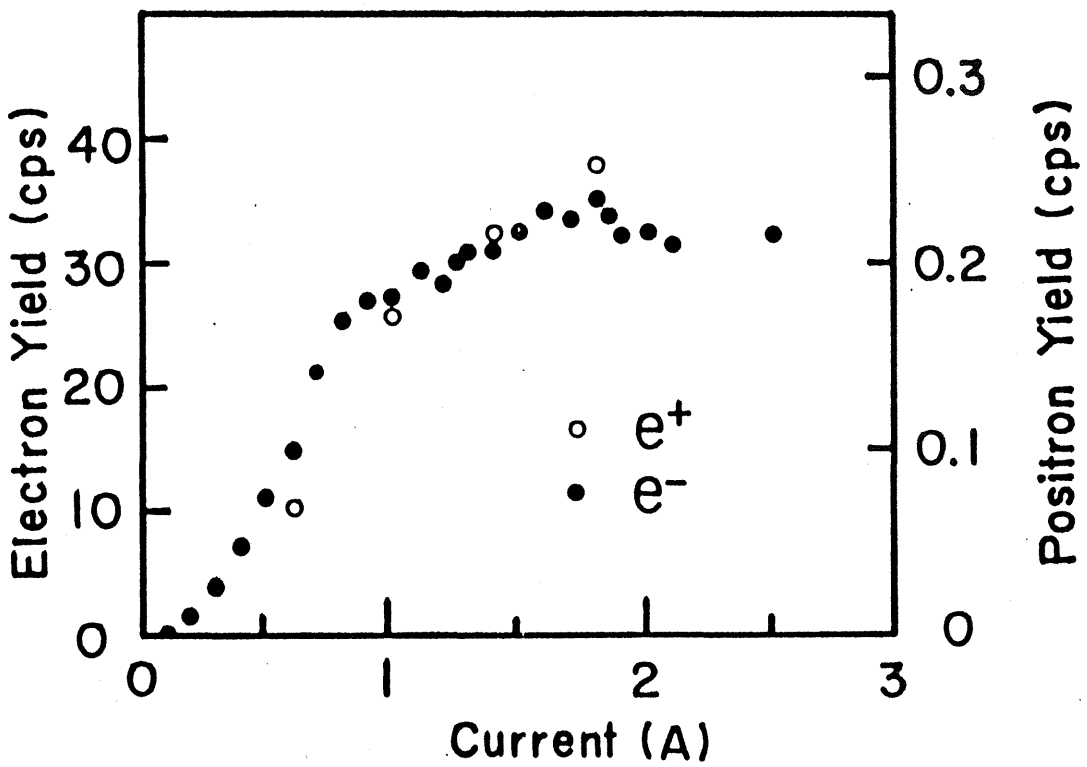

Fig. 10. Typical dependence of slow positron and electron yields on applied current for solenoid coil. The current 1 A corresponds to the axial magnetic field of 13 G.

secondary electrons ejected from the moderator depend on the field strength. The increase of intensity with the increase of field strength indicates that the beam becomes to include the positrons (electrons) with larger v_2. We made the TCS measurements in the field of 13 or 8 G.

F. Removal of Earth's and Stray Magnetic Field

As the strength of the guiding magnetic field should be weak to reduce several systematic errors, the earth's and stray magnetic fields, which tend to perturb the desired paths of slow positrons, should be also carefully minimized.

1. Stray magnetic field

Whole flight tube was made of 316 stainless steel, and was annealed for demagnetization after machining. All vacuum pumps, made of iron, were apart at least 2 m from the flight tube. Local magnetization still remained, but the magnitude is estimated to be a few mG at the spectrometer axis.

2. Earth's magnetic field

The flight tube was directed approximately parallel to the magnetic meridian line. Vertical and residual east-west components of the earth's magnetic field must be cancelled, while the component parallel to the axis simply acts as a part of the guiding field, and need not to be cancelled. For the present purpose μ-metal shielding is not suitable because

of the complexity of the piping. We adopted, therefore, the cancellation by Helmholtz coils (HC's).

The axis of helical trajectories of slow positrons is deflected from the spectrometer axis by the field perpendicular to the axial guiding field. At the end of the flight-path length ℓ, the deflection from the spectrometer axis, denoted as x, ammounts to

$$x = \ell \frac{B_2}{B_1} \quad , \tag{3}$$

where B_1 and B_2 are the axial and transverse components of the total magnetic field, respectively. Here the field is assumed to be uniform over the flight path. The value of x is required to be much smaller than the aperture radius 2 mm. To leave a sufficient margin, we ask $x < 0.1$ mm. When ℓ = 700 mm, Eq. (3) gives

$$B_2 < 1.4 \times 10^{-4} B_1 \quad . \tag{4}$$

Assuming that the practical lower limit of B_1 is 5 G, our goal of cancellation is

$$B_2 < 0.7 \text{ mG} \quad . \tag{5}$$

There may still exist several mG non-uniform and/or time-dependent magnetic fields, which cannot be removed by the static Helmholtz coils. However their effects to the beam deflection may be smaller than the uniform component, and may

tend to cancel one another. Hence it will be meaningful to aim at the intrinsic capability of HC's as Eq. (5).

As the vertical component of the earth's magnetic field is $\sim$ 300 mG, the non-uniformity of the magnetic field produced by the vertical HC should be within 0.2 % over the broad plane including the whole flight path. It is difficult for a conventional HC to achieve the expected uniformity, because too large size is required. Hence we adopted a double-pair-circular type HC (DHC) designed by Lee-Whiting.[21]

The principle of DHC is as follows. When two loops of electric current with radii a (m) and current J (A) are facing each other (see Fig. 11), the magnetic flux density in the plane $z = 0$ (the region of interest) is given by the Biot-Savart's law,

$$B_z = \frac{\mu_0 J}{\pi a} f(\rho) \quad ,$$

$$f(\rho) = \int_{-1}^{1} \frac{(1-\rho t)dt}{(1-t^2)^{1/2}(\rho^2+\delta^2+1-2\rho t)^{3/2}} \quad , \qquad (6)$$

$$\rho = r/a, \quad \delta = d/a,$$

$$B_r(r,\theta,0) = B_\theta(r,\theta,0) = 0 \quad .$$

The function $f(\rho)$ can be expanded as

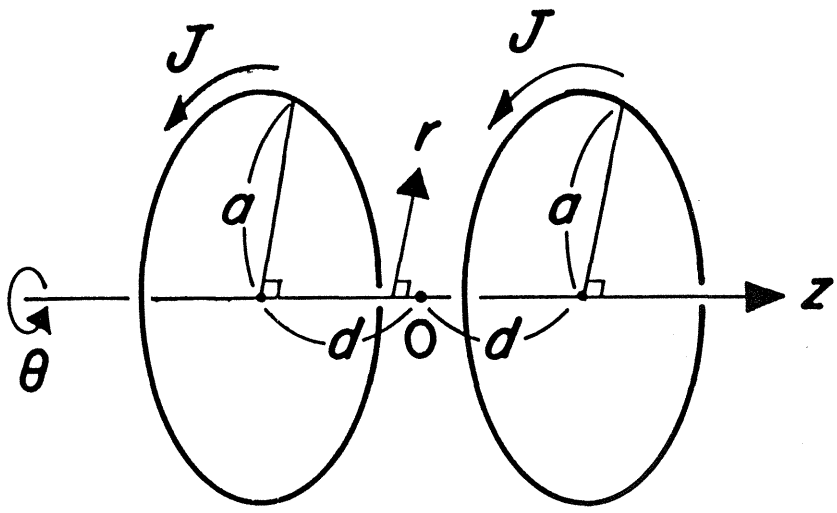

Fig. 11. Definition of coordinates and parameters for description of the magnetic field produced by Helmholtz coil.

$$f(\rho) = \sum_{i=0}^{\infty} \frac{\rho^{2i}}{(2i)!} f^{(2i)}(0) \quad . \tag{7}$$

First four $f^{(2i)}(0)$ are

$$\left.\begin{aligned} f(0) &= \pi(1+\delta^2)^{-3/2} \quad , \\ f^{(2)}(0) &= \pi(1+\delta^2)^{-7/2}(1.5-6\delta^2) \quad , \\ f^{(4)}(0) &= \pi(1+\delta^2)^{-11/2}(16.875-202.5\delta^2 \\ &\qquad +135\delta^4) \quad , \\ f^{(6)}(0) &= \pi(1+\delta^2)^{-15/2}(492.1875-11812.5\delta^2 \\ &\qquad +23625\delta^4-6300\delta^6) \quad . \end{aligned}\right\} \tag{8}$$

For a conventional HC δ is taken to be 0.5 so that

$$f^{(2)}(0) = 0 \quad .$$

Hence the non-uniformity of B_z comes from the fourth and higher order powers of ρ in Eq. (7). On the other hand, when another pair of current loops is added, the non-uniformity can be cancelled to the sixth order term (principle of the DHC).

The parameters of DHC, d/a, d'/a, and J'/J are given as functions of a'/a by several authors[21] (where the primes indicate that the values are for the additive pair of loops).

For the present DHC the parameters are chosen as

$$\left.\begin{aligned} &a = 1\ (m), \quad a' = 0.376\ (m), \\ &d = 0.390\ (m), \quad d' = 0.569\ (m), \\ &J'/J = 0.1\ . \end{aligned}\right\} \qquad (9)$$

For several sets of the parameters, $B_z(r)$ near $z=0$ plane was directly calculated by the Biot-Savart's law. The typical result is shown in Fig. 12. The uniformity of B_z is acceptable.

The east-west component, of which magnitude may be a few tens of mG at most, can be cancelled to a few tenth of mG with allowing 1% non-uniformity. Considering the accessibility to the chamber and the ease of construction, a single-pair-square type HC (SSHC) was adopted. For SSHC's, the best uniformity is obtained when[21]

$$d/a = 0.5444506\ , \qquad (10)$$

where a and d are a half of side length of squares and a half of distance between two squares, respectively. The present choice is

$$a = 1\ (m), \quad d = 0.544\ (m)\ . \qquad (11)$$

The configuration of coils are shown in Fig. 13.

A test of the HC system was made before installing them to the spectrometer. After adjustment of coil currents, it was confirmed that the residual magnetic field in the region concerned was several mG, mainly due to the inherent non-

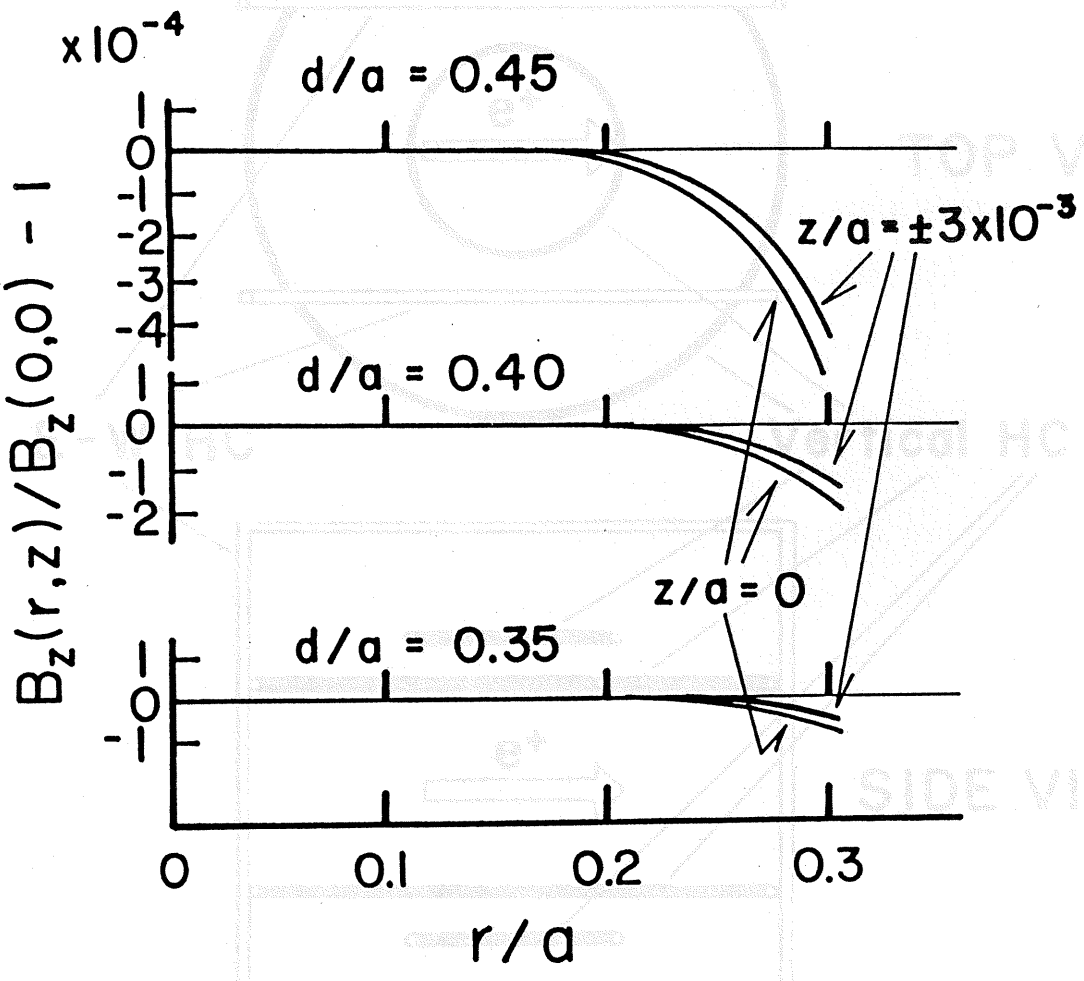

Fig. 12. Calculated magnetic field produced by double-pair-circular type Helmholtz coil near $z = 0$ plane.

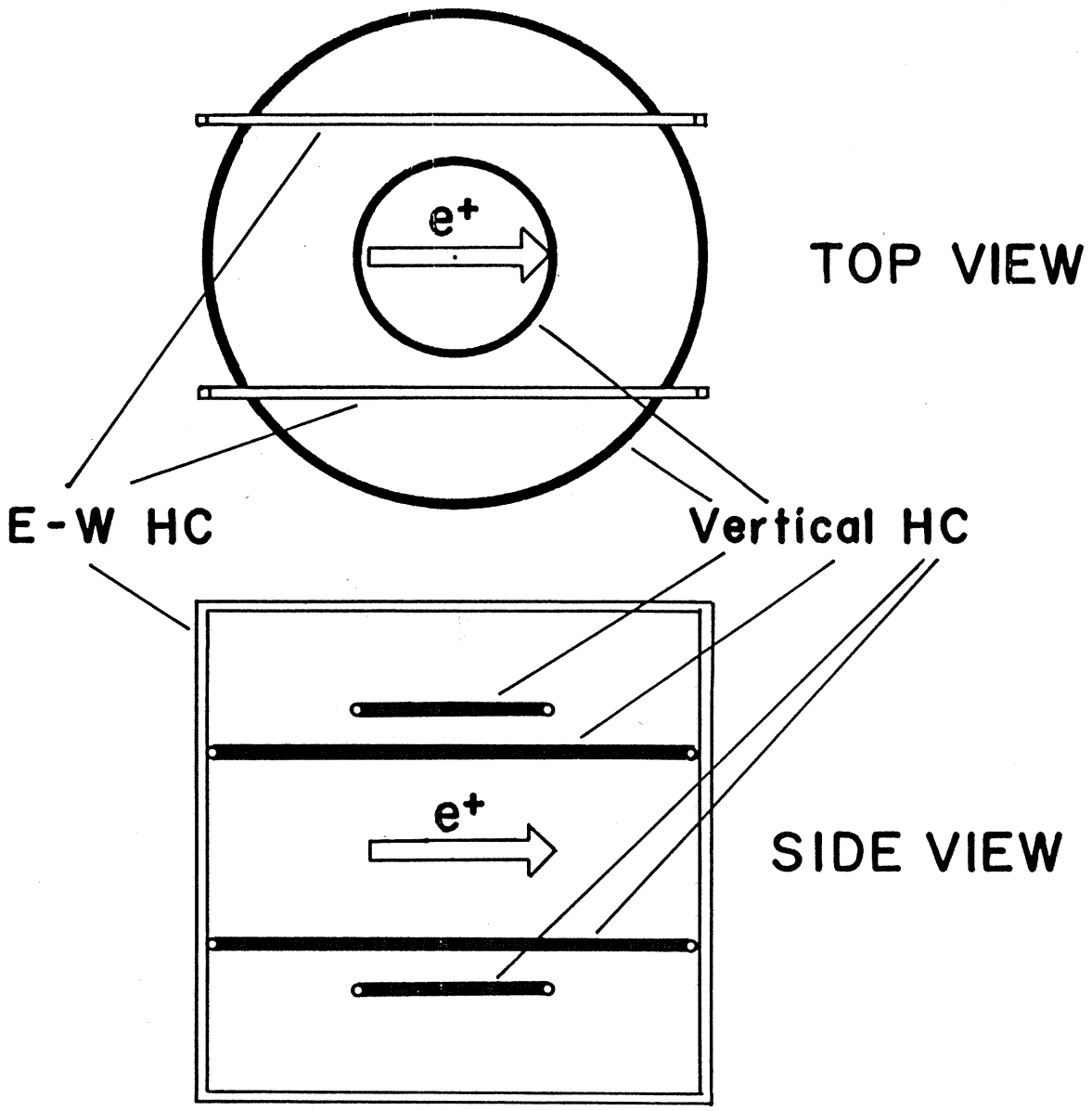

Fig. 13. Configuration of Helmholtz coils.
White arrows indicate positron flight path.

uniformity of the field to be cancelled.

3. Beam transmission test

After installation of the HC system, it is practically difficult to measure the magnetic field at the spectrometer axis. The adjustment of the currents for the HC's was done as follows. The beam intensity of slow positrons or electrons from the moderator was measured for the different setting of HC fields, and was plotted as a function of the applied fields. An example of such plots is shown in Fig. 14. A position of the maximum intensity was then determined, and was regarded as a position where the earth's magnetic field was cancelled. By the use of Eq. (3), the deflection of beam axis from the spectrometer axis can be related to the HC field as

$$x = \ell \frac{\vec{B}_2 - \langle \vec{B}_2 \rangle}{B_1} \quad , \qquad (12)$$

where $\vec{B}_2$ is the HC field, $\langle \vec{B}_2 \rangle$ is the HC field at the maximum beam intensity, and B_1 is approximately equal to the axial guiding field by the solenoid coil. In Fig. 14, it is seen that at x = 2 mm the beam intensity significantly decreases, as expected from the diameter of the apertures (4 mm), and that it is easy to suppress the beam deflection within several tenths of mm by maximizing the beam intensity.

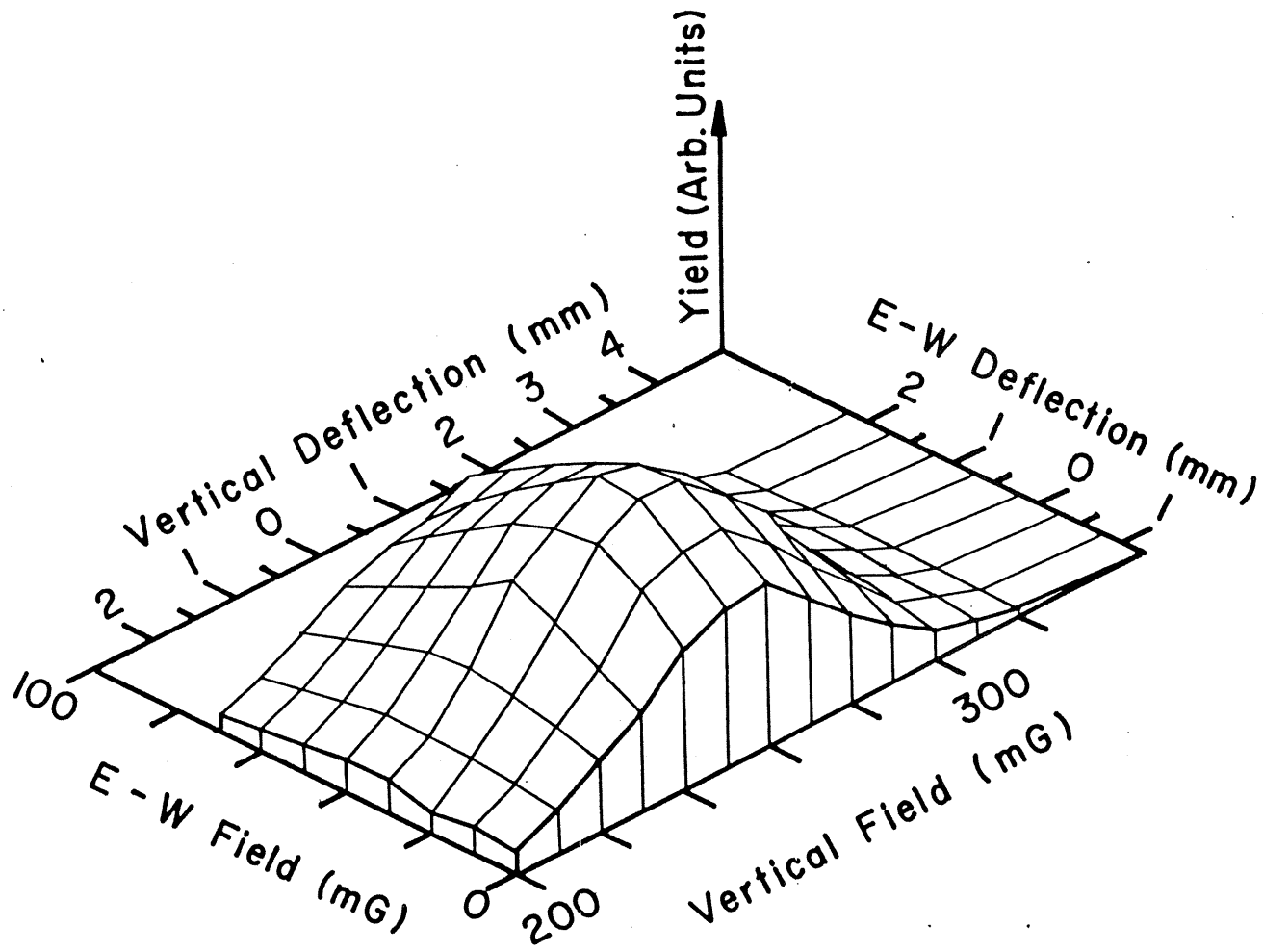

Fig. 14. Typical dependence of slow electron yields on applied HC fields.

G. Energy Determination

1. Principle

The whole flight path is divided into three regions, i.e., from the moderator to the grounded grid G_1; from G_1 to the grounded grid G_2; from G_2 to the MCP (see Fig. 15).

In the first region it is assumed that positrons are constantly accelerated by the uniform electric field applied between the moderator and G_1. Flight time in this region, t_0, is given by

$$t_0 = \left(\frac{m}{2e}\right)^{1/2} \frac{2d_0}{(E-V)^{1/2}+E^{1/2}} \quad , \qquad (13)$$

where E (eV) is the kinetic energy to be determined, V is the voltage applied to the moderator, and d_0 is the distance between the center of the moderator and G_1.

In the second region each positron flies with a constant velocity. Flight time in this region, t_1, is given by

$$t_1 = \left(\frac{m}{2e}\right)^{1/2} \frac{d_1}{E^{1/2}} \quad , \qquad (14)$$

where d_1 is the distance between G_1 and G_2.

The last region consists of two parts as shown in Fig. 15. The positrons passed G_2 are accelerated by the voltage V_M applied to the third grid G_3. From G_3 to the MCP the positrons fly with the kinetic energy $E + |V_M|$ (eV). Flight

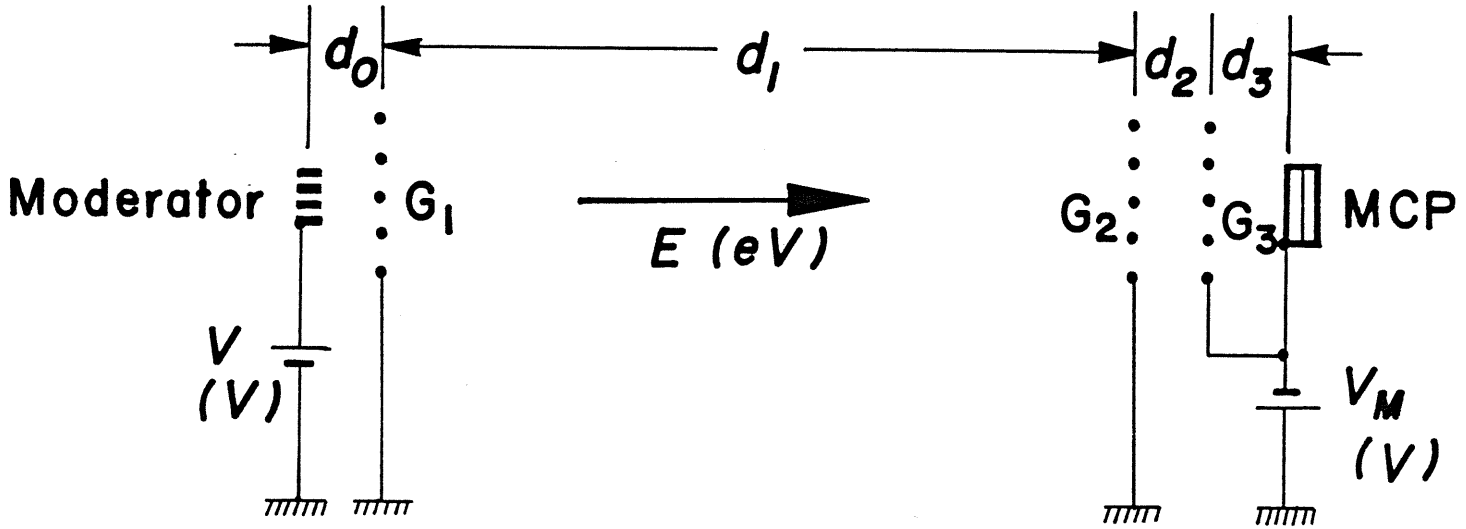

Fig. 15. Definition of parameters for energy determination.

time in this region, t_2 , is

$$t_2 = (\frac{m}{2e})^{1/2}[\frac{2d_2}{(E+|V_M|)^{1/2}+E^{1/2}} + \frac{d_3}{(E+|V_M|)^{1/2}}] \quad , \quad (15)$$

where d_2 and d_3 are the distances between G_2 and G_3, and between G_3 and the MCP, respectively. Considering $|E-V| << |V_M|$, this can be approximated without introducing a significant error as

$$t_2 = (\frac{m}{2e})^{1/2}[\frac{2d_2}{(V+|V_M|)^{1/2}+V^{1/2}} + \frac{d_3}{(V+|V_M|)^{1/2}}] \quad . \quad (16)$$

Hence t_2 can be regarded as a constant for each run.

Total flight time t is

$$t = t_0 + t_1 + t_2 \quad . \quad (17)$$

By using a channel number n,

$$t = \tau|n-n_0| + \frac{(d_0+d_1+d_2+d_3)}{c} \quad , \quad (18)$$

where τ is the channel width, n_0 is the center of prompt peak, and c is the velocity of light. Using Eqs. (13), (14), (16), (17), and (18), E can be determined as a function of n.

2. Accuracy of energy determination

The errors in energy determination associated with the parameters in above equations can be estimated as follows. Assuming

$$V \cong E, \qquad E \ll |V_M| , \tag{19}$$

Eq. (17) reduces to

$$t \sim (\frac{m}{2e})^{1/2} \frac{2d_0+d_1}{E^{1/2}} . \tag{20}$$

Hence

$$E \sim \frac{m}{2e}(\frac{2d_0+d_1}{t})^2 ,$$

$$\sim \frac{m}{2e} \frac{(2d_0+d_1)^2}{\tau^2(n-n_0)^2} . \tag{21}$$

Finally, we get

$$\frac{\Delta E}{E} \sim \frac{2|\Delta\tau|}{\tau} + \frac{2|\Delta n_0|}{|n-n_0|} + \frac{2(2|\Delta d_0|+|\Delta d_1|)}{2d_0+d_1} , \tag{22}$$

where Δ means the systematic error associated to each quantity. The upper estimate for each term is

$$\frac{2|\Delta\tau|}{\tau} \lesssim \begin{cases} 0.8\ (\%) & \text{for } V \geq 3\ (V) \\ 2\ (\%) & \text{for } V < 3\ (V) \end{cases} ,$$

$$\left.\begin{aligned} \frac{2|\Delta n_0|}{|n-n_0|} &\lesssim \frac{100}{|n-n_0|}\ (\%) \quad , \\ \frac{2(2|\Delta d_0|+|\Delta d_1|)}{2d_0+d_1} &\lesssim 1.8\ (\%) \quad , \end{aligned}\right\} \qquad (23)$$

where numerical values used are,

$$\frac{|\Delta\tau|}{\tau} \lesssim \begin{cases} 0.4\ (\%) & \text{for } V \geq 3\ (V) \\ 1.0\ (\%) & \text{for } V < 3\ (V) \end{cases} \quad ,$$

$$|\Delta n_0| \lesssim 0.5 \quad , \qquad (24)$$

$$d_0 = 10\pm1\ (mm),\ d_1 = 661\pm4\ (mm) \quad .$$

In the following subsection, it will be shown, by the observation of well-known electron-molecule resonances, that the actual error is much smaller than the estimated from Eq. (23).

Another error in energy determination is caused by the helical motion of positrons in the axial magnetic field. Total kinetic energy of a positron is expressed as

$$E = \frac{1}{2}mv_1^2 + \frac{1}{2}mv_2^2 \quad , \qquad (25)$$

where v_1 and v_2 are the axial and transverse components of velocity. The second term is usually neglected in the TOF method. When the axial magnetic field is applied, however, v_2

may become significantly large because of the spiralling, and a priori neglection of v_2 cannot be justified. The upper limit of the second term can be estimated by the use of Eq. (2), as

$$\frac{1}{2}mv_2^2 < \frac{(eBR)^2}{2m} \qquad (26)$$

Substituting R = 1 (mm), the second term for the present spectrometer is less than 0.15 eV for B = 13 G and 0.06 eV for B = 8 G. The distribution of the value of second term for each positron causes one of restrictions on energy resolution of the system, and the mean value appears as the shift of energy scale. Practically the latter is several times smaller than the upper limit.

The other errors, due to the factors which are not explicitly contained in the equations for energy determination, are mainly caused by: (a) contact potential differences; (b) charging of insulators; (c) finite time interval between a β-decay and a re-emission of slow positron from the moderator. Although definite evaluation of these errors is difficult, there are several reasons which permit us to neglect them, at least in the energy range studied in this work. The most demonstrative evidence is provided by the observation of the electron resonances.

3. Observation of electron-N_2 and -He resonances

An overall check of the energy determination is performed

by the observation of two well-known resonances, i.e. e^--N_2 around 2 eV and e^--He resonance at 19.36 eV, by using slow secondary electrons ejected from the moderator. These resonances are located near both boundaries of the energy region which is covered in the present measurement of the positron-helium TCS, and therefore provide good standard for the check of energy scale. Experimental procedure and data analysis were essentially the same as those for the measurement of the positron TCS's (see below), although the absolute determination of TCS's was not made because of the difficulties related to much larger TCS's of e^--N_2 and -He than e^+-He, e.g. difficulty of gas handling.

The observed energy dependences of the TCS's of e^--N_2 and e^--He are shown in Figs. 16 and 17, respectively. The present results for e^--N_2 are normalized to the result of Kennerly's[22] at 1 eV. Observed location of the fine structure of the resonance agrees to Kennerly's within a few tens of meV. Hence the error in the present energy scale is a few percents at these energies. The resonance of e^--He was observed at 19.2 eV. As the most reliable location at present is believed to be 19.361 ± 0.009 eV,[23] the error is 1 % at this energy.

In both cases, the positions of resonances were not appreciably deviated by the change of the axial magnetic field. This suggests that the second term of the right side

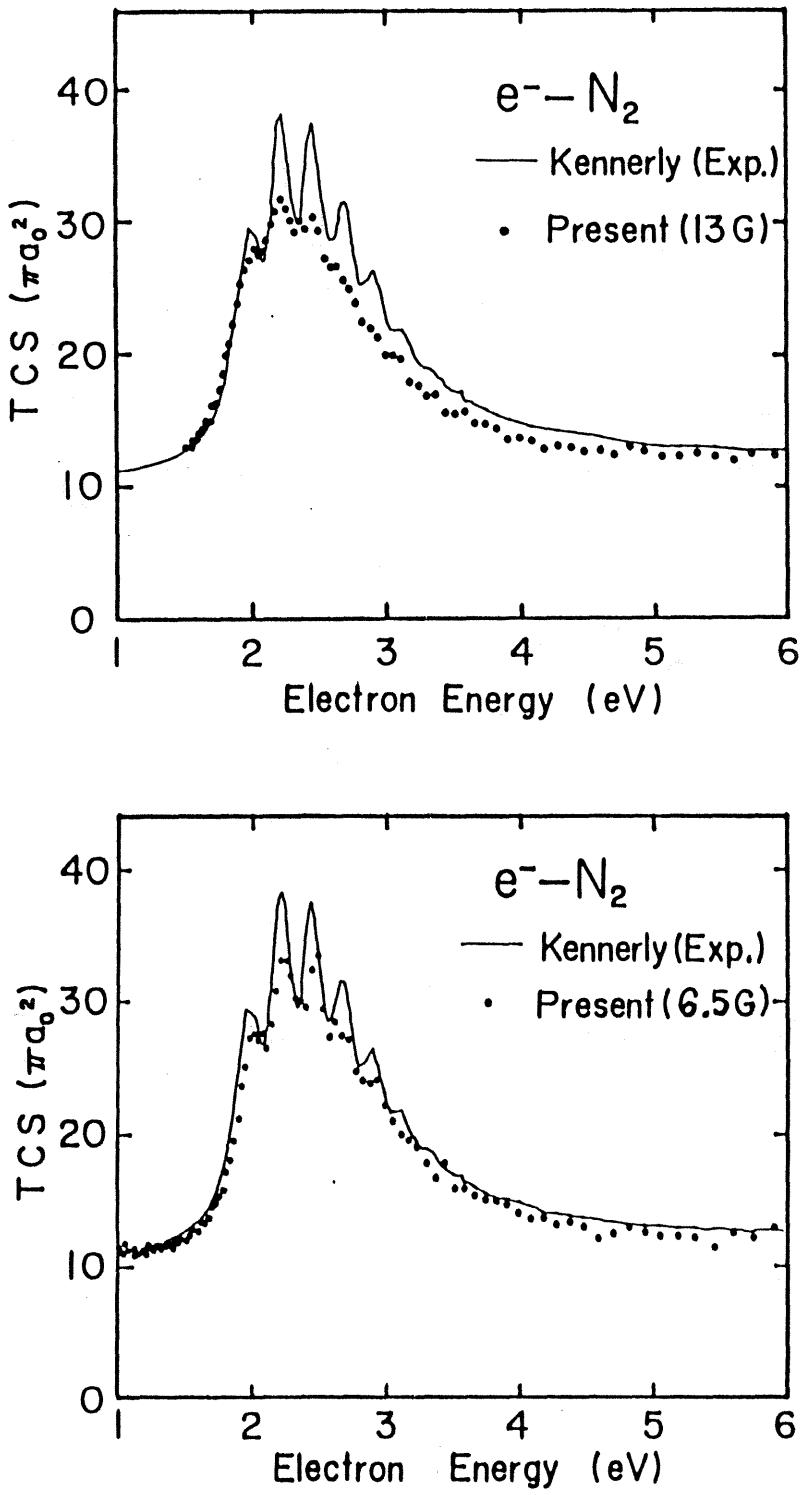

Fug. 16. Measured energy dependence of electron-nitrogen total cross sections. Present results are normalized to Kennerly's results at 1 eV.

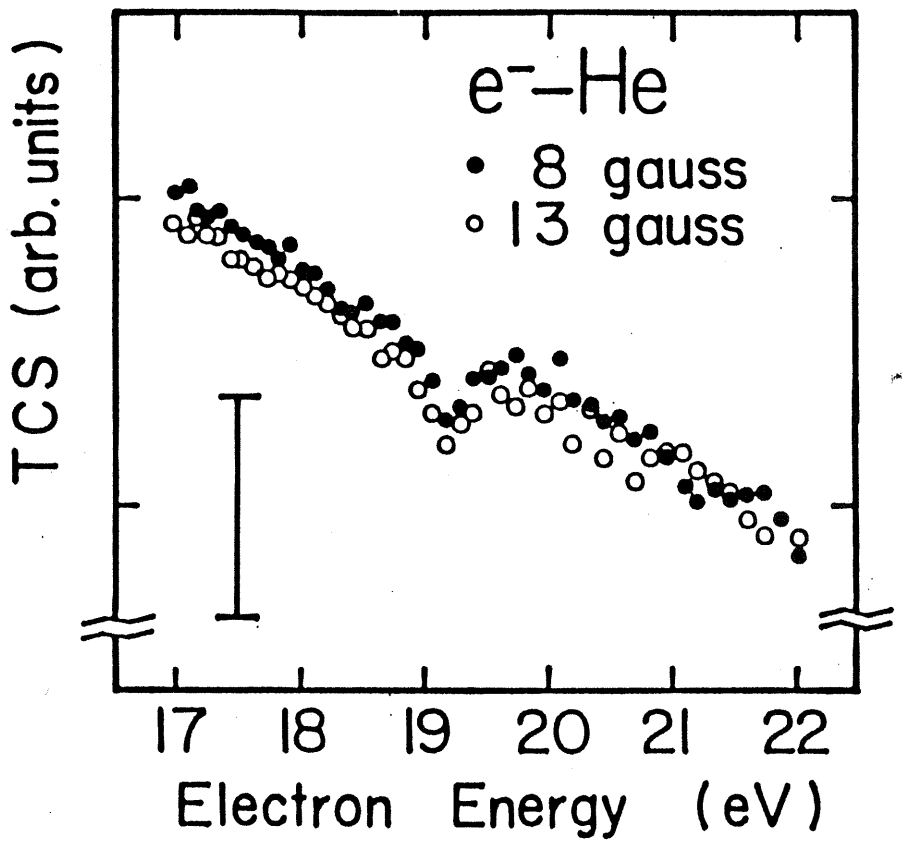

Fig. 17. Measured energy dependence of electron-helium total cross sections. The vertical bar represents 10 % of the TCS at the midpoint of the bar.

of Eq. (25) does not cause significant shift of energy scale, when the strength of the axial field is less than ∿13 G. There is no reason to suspect that this is not true for the positron case.

The observed slight error can be explained by

(*a*) ∿0.4% underestimate of $\tau/(2d_0+d_1)$, due to underestimate of τ and/or overestimate of $(2d_0+d_1)$

or (*b*) 1 nsec error in t due to the error in n_0 and/or neglected time interval between the β-decay and the electron emission from the moderator.

Both are within the estimated ranges of possible errors discussed in the previous subsection.

In conclusion, the error in the present energy determination is acceptably small in the energy range of our interest, although the error may increase for the higher energy region.

4. Energy resolution

The main purpose of the present work is to refine positron-helium TCS's especially near the Ramsauer minimum, where the TCS varies rapidly with energy. Poor energy resolution causes overestimate of the TCS's around the minimum, for the observed TCS is the mean value over the width of energy resolution. Therefore the resolution of the

present spectrometer should be carefully examined.

In a future work the present spectrometer can be used for searching *resonances* in positron-atom or -molecule scattering, which have not so far been observed. This is the second reason to discuss the resolution in detail.

The energy resolution of the present TOF spectrometer is determined mainly by three factors, i.e. the time resolution, the uncertainty of flight path length (mainly due to the width of moderater along the axial direction), and the uncertainty of the additive kinetic energy due to the transverse component of velocity (the second term of the right side of Eq. (25)). The overall resolution ΔE can be expressed as a root-sum-squares of three factors.

When the three factors are denoted as ΔE_t, ΔE_d, and ΔE_2,

$$\left.\begin{aligned} \Delta E &= [(\Delta E_t)^2+(\Delta E_d)^2+(\Delta E_2)^2]^{1/2} \quad , \\ \Delta E_t &= \frac{2\Delta t}{t}E \quad , \\ \Delta E_d &= \frac{2(2\Delta d_0+\Delta d_1)}{2d_0+d_1}E \quad , \\ \Delta E_2 &\lesssim \frac{(eBR)^2}{2me} \quad [eV] \quad . \end{aligned}\right\} \qquad (27)$$

where Δt, Δd_0 and Δd_1 are not systematic errors as in Eq. (22), but the widths of the statistical distributions of the

related quantities for many positrons. The inequality for the last factor ΔE_2 is the same as Eq. (26). Using the actual conditions

$$\Delta t = 1.2 \text{ (nsec)}, \quad \Delta d_0 = 2 \text{ (mm)}, \quad \Delta d_1 = 0 , \quad R = 1 \text{ (mm)}, \tag{28}$$

ΔE_t, ΔE_d, and ΔE_2 are evaluated (see Fig. 18). At several electron volts, ΔE_2 is dominant, as confirmed by the measurement of the e^--N_2 resonance in two different strengths of B (see Fig. 16). On the other hand, near the e^--He resonance these three factors are comparable, and the change in B does not significantly affect the overall resolution as seen in Fig. 17.

In conclusion, Fig. 18 shows that the overall resolution is good enough for the present purpose. Especially at several eV the resolution less than 0.1 eV is attainable by reducing B. For the study of resonance in the higher energy region, however, somewhat better resolution is required.

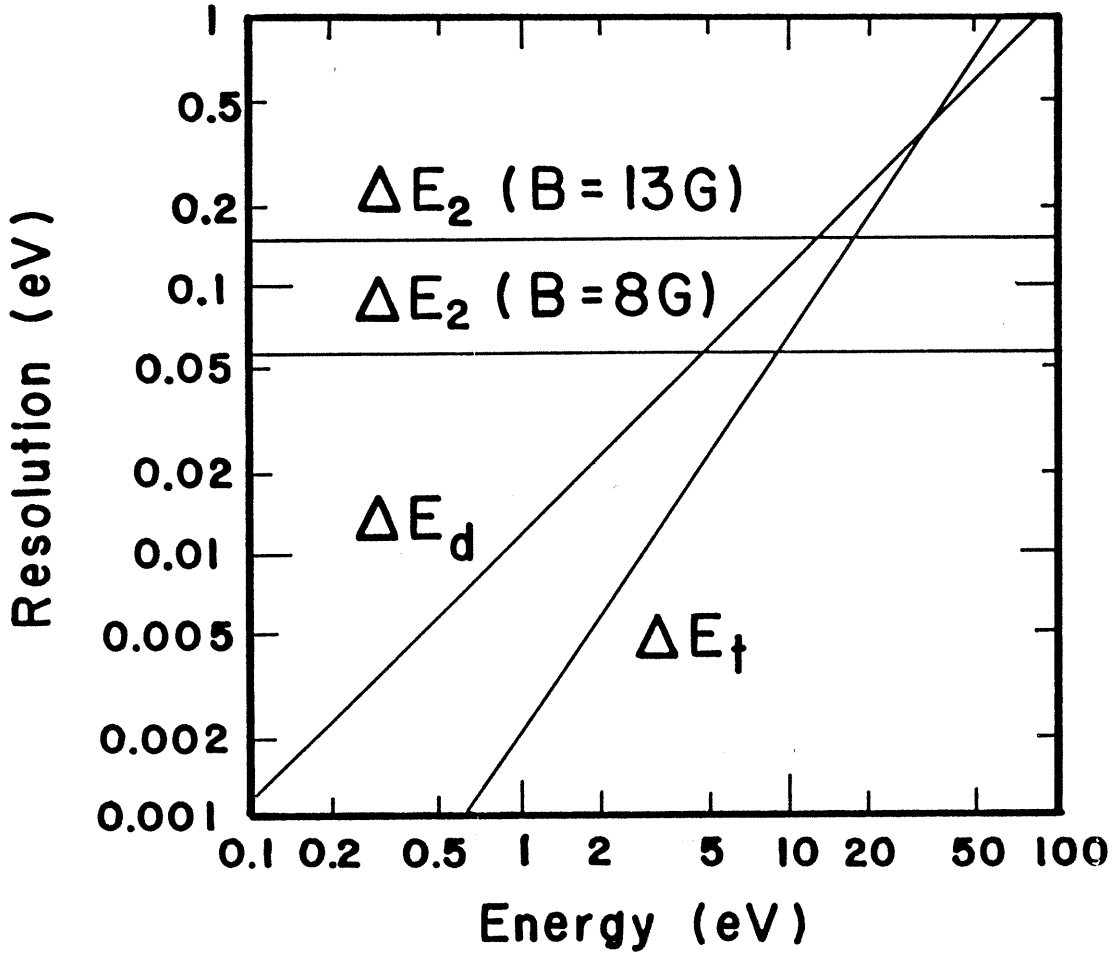

Fig. 18. Energy resolution of the present spectrometer. Definitions of ΔE_t, ΔE_d, and ΔE_2 are given in the text.

CHAPTER III

EXPERIMENTAL PROCEDURE AND DATA ANALYSIS

A. Outline

The present experimental conditions to measure positron-helium total cross sections (TCS's) are tabulated in Table 1. The energy range from 0.6 to 22 eV was covered, and for some energy regions several independent measurements under different experimental conditions were performed in order to examine systematic errors, if any.

The TCS, denoted as σ, is determined from the equation

$$\sigma = \left(\int \rho(\ell) d\ell\right)^{-1} \ln(n_v/n_g) \ , \qquad (29)$$

where n_v and n_g are the count rates of positrons fallen into the corresponding energy-bins of the "vacuum" and "gas" spectra, respectively. The number density of helium atoms at a point ℓ on the flight path is denoted as $\rho(\ell)$. The integration is taken over the whole flight path.

A "run" consists of measurements of three spectra, i.e. two time-of-flight (TOF) spectra ("vacuum" and "gas") and "calibration" for random coincidence correction. Extremely long accumulation time is required for each "run" because of the weakness of the incident beam, and may possibly introduce appreciable variation of the beam intensity during the "run".

Table 1. Experimental conditions.

Axial magnetic field strength[a] (gauss)	Acceleration voltage (volt)	Gas pressure[b] (Torr)
8	-0.5, 0.5	0.12
13	-1.0, 0, 1.0, 3.0	0.12
13	3.0, 4.0, 7.0, 10.0, 13.0, 15.0, 17.0, 18.5, 20.0	0.06
o	15.0, 16.5, 18.5, 19.5	0.06
8	19.5	0.04

a. Measured at the cylindrical aperture in front of the MCP.

b. Measured at the gas cell.

In order to minimize the error due to the change in beam intensity, each "run" except for the "calibration" measurement was divided into 8 to 16 short "segments". Each "segment" consists of two alternate periods for "vacuum" and "gas" spectra. A typical length of a "segment" was a day or half a day, and the sharing ratio of time between "vacuum" and "gas" was typically 1:2. After the whole measurements of a "run", $ln(N_v/N_g)$, where N_v and N_g are the numbers of detected slow positrons during the "vacuum" and "gas" period respectively, was calculated for each "segment" in order to check the effect of the intensity drift. When the standard deviation of the values throughout the "run" was much larger than the expected statistically, the whole data of the "run" were discarded.

Since the decay of ^{22}Na source during several "runs" is not negligible, a "calibration spectrum" for random coincidence correction[24] was measured at the middle of each "run". The "vacuum" and "gas" spectra summed over all the "segments" in the "run" are processed with the "signal restoration" procedure, by using the "calibration" data.

The "restored" TOF spectra are then converted to energy spectra, from which the TCS for each energy bin is deduced by the use of Eq. (29). Since the slow positron peak in each spectrum has about 2 eV width, the TCS's within this width can be determined simultaneously.

When the magnetic field was set to 8 G, the "run" was repeated several times, in order to reduce statistical uncertainties. In these cases, the final TCS's were deduced by averaging the results of each "run" with the weights of the inverse squares of statistical uncertainties.

Some pairs of different "runs" partially overlap in their energy region. The comparison of the TCS's in the overlapped energy region is a good probe for a check of data. It was confirmed that the TCS's were consistent within the statistical uncertainties as far as the strength of magnetic field was identical (see Fig. 19). Hence the TCS's in the overlaps with same field strength were averaged to obtain the final results. (The difference between two sets of TCS's with different field strength contains some information on forward scattering and spiralling.)

B. "Segmentation" of Data Accumulation

In the transmission method the uniformity of beam intensity is of essential importance, for the "vacuum" spectra (to measure *beam intensity*) and the "gas" spectra (to measure *attenuation*) are *alternately* accumulated. "Segmentation" of each "run" enables us not only to check the intensity periodically but also to minimize the influence of the possible intensity drift on the accuracy of TCS.

For a typical "run", the observed counts of slow

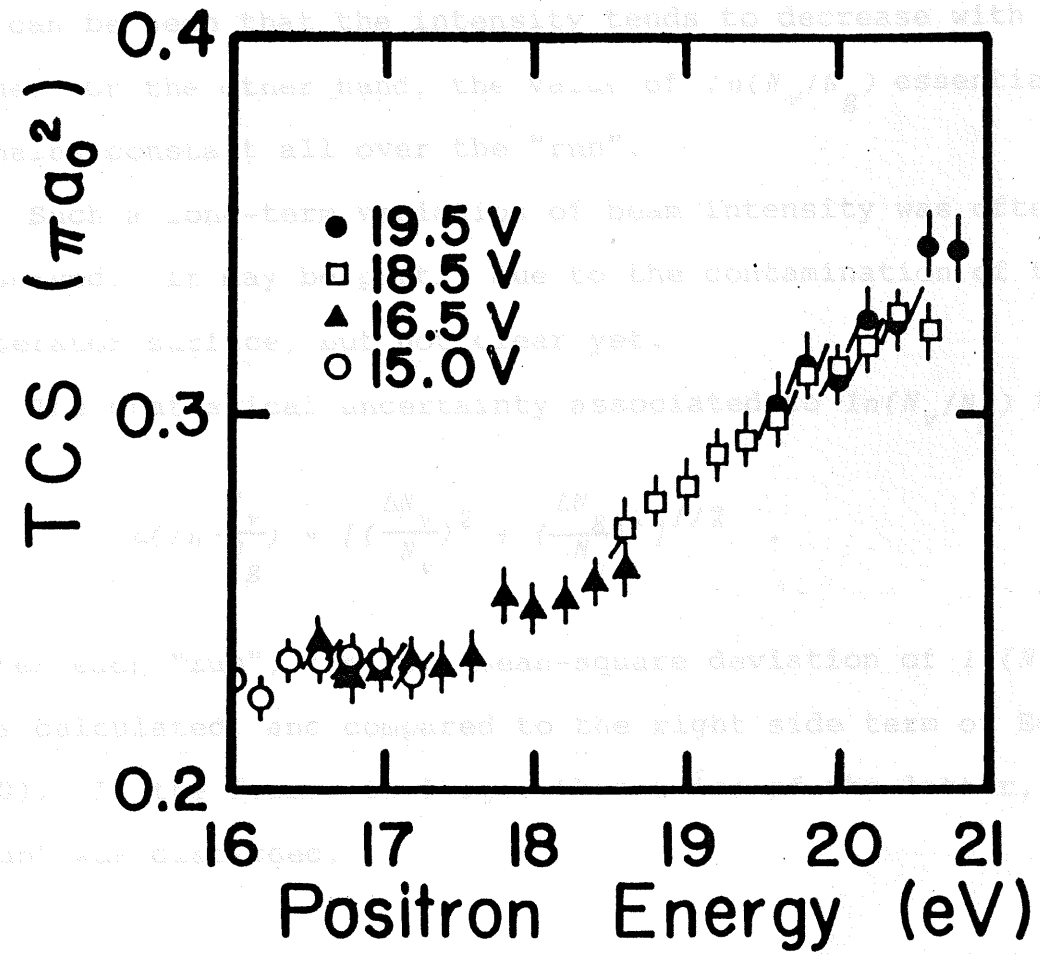

Fig. 19. Comparison of the TCS's measured with different acceleration voltages. Axial magnetic field 8 G was applied for each run.

positrons in the "vacuum" and the "gas" period of each "segment" are plotted against the elapsed time (see Fig. 20). It can be seen that the intensity tends to decrease with time. On the other hand, the value of $ln(N_v/N_g)$ essentially remains constant all over the "run".

Such a long-term variation of beam intensity was often observed. It may be partly due to the contamination of the moderator surface, but not clear yet.

The statistical uncertainty associated to $ln(N_v/N_g)$ is

$$\Delta(ln\frac{N_v}{N_g}) = [(\frac{\Delta N_v}{N_v})^2 + (\frac{\Delta N_g}{N_g})^2]^{1/2} \quad . \qquad (30)$$

After each "run", the root-mean-square deviation of $ln(N_v/N_g)$ was calculated, and compared to the right side term of Eq. (30). If the former is larger than twice of the latter, the "run" was discarded.

C. Allowance for random coincidence

After acceptance of a start pulse by the time-to-amplitude convertor (TAC), the measuring process can be accidentally terminated by an unrelated stop pulse prior to the real stop pulse. In such a case the output of the TAC is stored in a channel of the MCPHA memory corresponding to the shorter time interval than that between the true start and

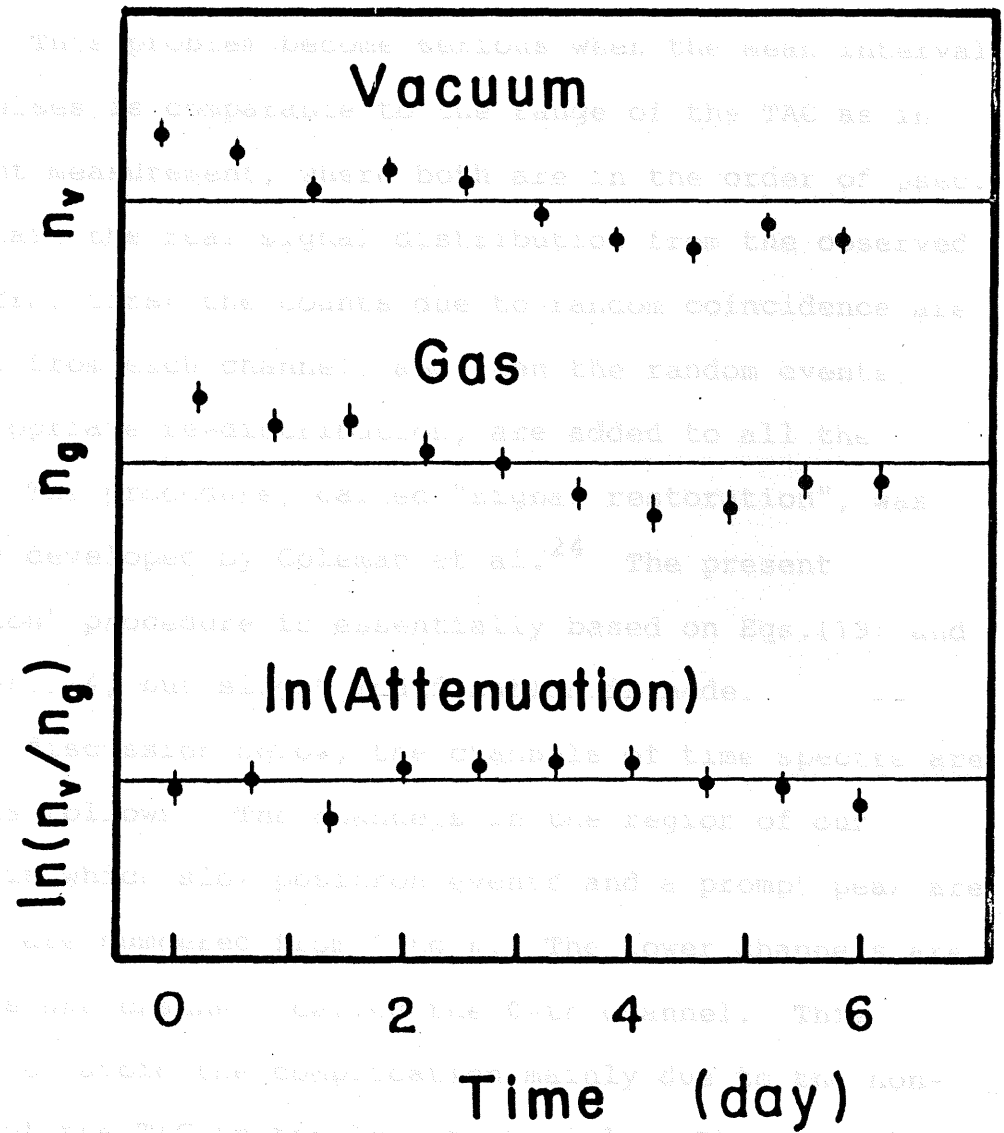

Fig. 20. Drift of slow positron yield for a typical run.

stop signals. This forms the "random background" in the TOF spectrum. This problem become serious when the mean interval of stop pulses is comparable to the range of the TAC as in the present measurement, where both are in the order of μsec.

To obtain the real signal distribution from the observed time spectra, first the counts due to random coincidence are subtructed from each channel, and then the random events, after appropriate re-distribution, are added to all the channels. The procedure, called "signal restoration", was originally developed by Coleman et al.[24] The present "restoration" procedure is essentially based on Eqs.(19) and (20) of Ref. 24, but slight modification is made.

In the discussion below, the channels of time spectra are numbered as follows. The channels in the region of our interest, in which slow positron events and a prompt peak are contained, are numbered from 1 to n. The lower channels are regarded as *one* channel, called the 0-th channel. This enables us to avoid the complication mainly due to the non-linearity of the TAC in the lowest channels. The channels higher than n and the region out of the TAC range are also combined to one channel, numbered $n+1$.

The probability of random coincidence to the i-th channel, i.e., the probability with which the events belonging to higher channels fall into the i-th channel by random "stop" pulses, is denoted as p_i. The probabilities

are determined from a "calibration" spectra, which is measured at the meantime of a "run" with 60 Hz regularly spacing start pulses and randomly distributed stop pulses from the photomultiplier. In principle,

$$p_i = C_i/N \quad , \tag{31}$$

where C_i is the counts in the i-th channel of the "calibration" spectra, and N is the total counts of "valid start" signals. Practically, p_i is approximated as

$$p_i = A \cdot exp(-Zi) \qquad (1 \leqq i \leqq n) \quad , \tag{32}$$

and the parameters A and Z are determined by the use of least-squares method. For p_0, Eq. (31) was used, and p_{n+1} is determined by

$$p_{n+1} = 1 - \sum_{i=0}^{n} p_i \quad . \tag{33}$$

In the "vacuum" and "gas" measurements, true spectrum S_i can be related to the observed spectrum D_i as

$$D_i = (1 - \sum_{j=0}^{i-1} p_j)S_i + p_i(N_1 - \sum_{j=0}^{i} S_j) \quad , \tag{34}$$

where N_1 is the observed total counts of "valid start" signals.

$$N_1 = \sum_{i=0}^{n+1} D_i = \sum_{i=0}^{n+1} S_i \quad . \tag{35}$$

From Eq. (34),

$$S_i = (1-\sum_{j=0}^{i} p_j)^{-1}[D_i - p_i(N_1 - \sum_{j=0}^{i-1} S_j)] \quad , \qquad (36)$$

which corresponds to Eq. (20) of Ref. 24. With this equation, we get S_i's successively from the 0-th channel.

Statistical errors for S_i's are calculated as follows. The observed counts D_i's ($0 \leq i \leq n+1$) are statistically independent one another, and S_i's can be expressed as linear combinations of D_i's. Defining coefficients $k_j^{(i)}$ by

$$\sum_{j=0}^{i} S_j = \sum_{j=0}^{n+1} k_j^{(i)} D_j \quad , \qquad (37)$$

Eq. (36) reduces to

$$S_i = \sum_{j=0}^{n+1} c_j^{(i)} D_j \quad , \qquad (38)$$

where

$$c_j^{(i)} = (1-\sum_{\ell=0}^{i} p_\ell)^{-1}[\delta_{ij} - p_i(1-k_j^{(i-1)})] \quad . \qquad (39)$$

Hence the statistical error ΔS_i is given by

$$\Delta S_i = [\sum_{j=0}^{n+1} (c_j^{(i)})^2 D_j]^{1/2} \quad . \qquad (40)$$

The coefficients $k_j^{(i)}$ can be determined successively from $i=0$ by

$$k_j^{(0)} = \begin{cases} 1 & (j=0) \\ -p_0/(1-p_0) & (j\ 0) \end{cases} , \qquad (41a)$$

$$k_j^{(i+1)} = k_j^{(i)} + c_j^{(i+1)} . \qquad (41b)$$

An example of the "signal restoration" is demonstrated in Fig. 21.

D. Conversion to Energy Spectrum

The TOF spectra proccessed with the "signal restoration" procedure are then converted to "energy spectra" prior to the TCS determination. Several consecutive channels in a proccessed TOF spectrum are suitably combined so as to form constant bin-widths in energy spectrum. The events in the TOF channel corresponding to a certain bin-boundary are appropriately shared by the two neighboring energy-bins.

E. Evaluation of Target Thickness

To determin the TCS's by using Eq. (29), the factor $\int \rho(\ell) d\ell$, i.e. "target thickness" should be evaluated. From the Boyle Charles' law, one gets

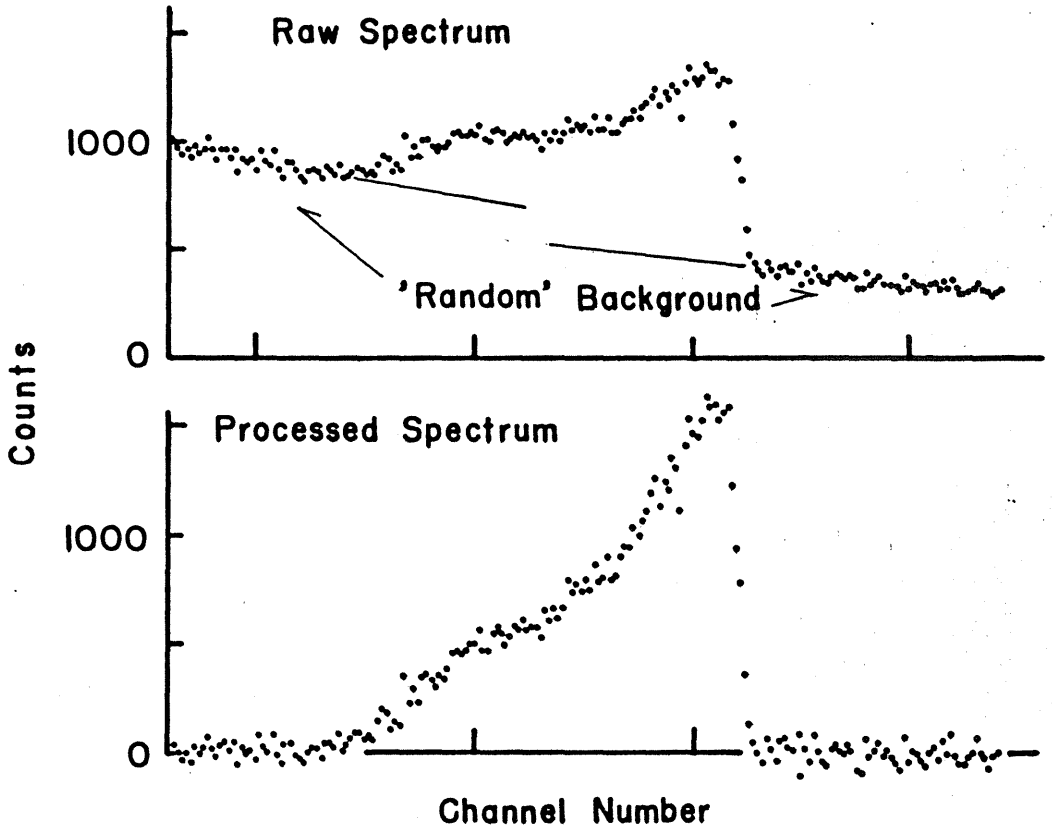

Fig. 21. Example of "signal restoration". The spectrum was obtained with 1-V acceleration in 13-G axial magnetic field. 6.30 nsec/channel.

$$\int \rho(\ell) d\ell = (k_B T)^{-1} \int P(\ell) d\ell \quad , \tag{42}$$

where k_B is the Boltzmann constant, T is the temperature of target gas, and $P(\ell)$ is the pressure at the point ℓ. The integral, in principle, is taken over the whole flight path. In the actual measurements, however, the pressure can be determined only at several points described in CHAPTER II, and hence suitable approximation for pressure distribution should be adopted. Furthermore, due to the difference between the temperatures of the manometer sensor head (regulated at 45°C) and of the gas cell, the "thermal transpiration" effect must be taken into account to correct the pressure.

1. Pressure distribution

The integral $\int P(\ell) d\ell$ is approximated by

$$\int P(\ell) d\ell = P_1 \ell_1 + P_2 \ell_2 \quad , \tag{43}$$

where P_1 and P_2 are the pressures at and out of the gas cell respectively, and ℓ_1 and ℓ_2 are the "effective lengths" of the regions where the pressures are P_1 and P_2, respectively. The parameters ℓ_1 and ℓ_2 are determined as follows. In and out of the gas cell, the pressure is assumed to be constant; in the cylindrical apertures, the pressure is assumed to change linearly (see Fig. 22). Using the numerical values given in Fig. 22, one finds

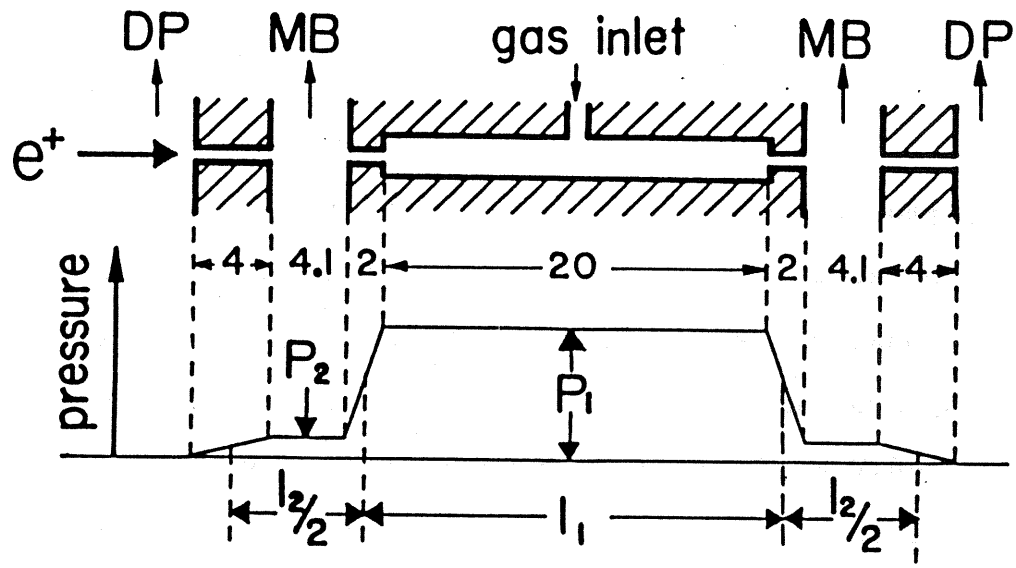

Fig. 22. Assumed pressure distribution for evaluating target thickness. MB, mechanical booster pump; DP, oil diffusion pump. Numerical values are the lengths of associated parts in cm.

$$\ell_1 = 22\ (cm)\ ,\ \ell_2 = 14.2\ (cm)\ . \qquad (44)$$

The resultant contribution of $P_2\ell_2$ to the integral $\int P(\ell)d\ell$ is less than 10 %.

2. Thermal transpiration

The pressure out of the gas cell (P_2) is so small that the thermal transpiration correction for P_2 does not cause appreciable change in the evaluated target thickness. Here we discuss the correction for the pressure in the gas cell.

Pressure used in the present work is from 0.04 to 0.12 Torr, where the Liang-type equation[25] is suitable.

$$\frac{P}{P'} = \frac{R_m+\alpha\phi(DP')+\beta\phi^2(DP')^2}{1+\alpha\phi(DP')+\beta\phi^2(DP')^2}\ , \qquad (45)$$

where P and P' are true and observed pressures, respectively. The parameter ϕ is 1 for helium, and D, the diameter of the tube connecting the sensor and the gas cell, is 6 mm. The empirical parameters α and β are chosen as[26]

$$\left.\begin{aligned}\alpha &= 2.13\ ,\\ \beta &= 4.82[1-(T/T')^{1/2}]\ ,\end{aligned}\right\} \qquad (46)$$

where T and T' are the temperatures at the gas cell and the sensor, respectively.

The low pressure limit of the correction factor, R_m, was

reported[22,26,27] to be considerably different from the theoretical value $(T/T')^{1/2}$. For a capacitance manometer, several authors reported[22,27] that the observed values of $1-R_m$ is about a half of $1-(T/T')^{1/2}$. R_m may be seriously affected by the geometrical configuration around the sensor head. Since we have no means of direct measurement of R_m in the present work, we tentatively adopted the average of "full" and "no" correction

$$R_m = \frac{1}{2}[1+(T/T')^{1/2}] \quad . \tag{47}$$

This gives approximately the same R_m as several groups whose configurations around the sensor are similar to ours. There does not exist, of course, sufficiently convincing evidence to support this choice. Therefore a systematic error may possibly be introduced, and in the worst case it may amount to the same order of magnitude as the correction itself. The resultant correction to the TCS is, however, no more than 0.8, 1.2, and 1.5 % for P_1= 0.12, 0.06, and 0.04 Torr respectively, where T = 24°C.

The observed temperature at the gas cell was from 20 to 28°C. In this range the correction factor does not change significantly, and the values for T= 24°C were used throughout all the measurements in the present work.

3. Conclusion

In conclusion, the target thickness is calculated by

$$\int \rho(\ell)\,d\ell = \begin{cases} (k_B T)^{-1}(21.8P_1' + 14.0P_2') \\ \qquad (\text{for } P_1' = 0.12 \text{ Torr}) \\ (k_B T)^{-1}(21.7P_1' + 14.0P_2') \quad , \\ \qquad (\text{for } P_1' < 0.06 \text{ Torr}) \end{cases} \tag{48}$$

where P_2' was determined as a function of P_1' (see Fig. 7).

CHAPTER IV

DISCUSSION ON ERRORS IN TCS

An overall check of energy scale was made by means of the electron resonances as described in CHAPTER II. It has been revealed that no significant error in energy scale exists. Discussion in this chapter is focussed on the errors in total cross sections (TCS's).

A. Target Thickness

Here the errors associated with the parameters in target thickness are discussed.

1. Temperature drift

The drift of gas temperature during each "run" was within ± 2 K, which results in ± 0.7 % of error at maximum in the TCS.

2. Errors in pressure measurements

The quoted scale accuracy of the manometer is 0.08 %. Sensor zero drift was found to be within 1×10^{-4} Torr, which results in 0.08, 0.16, and 0.25% error at maximum in the TCS for P_1 = 0.12, 0.06, and 0.04 Torr, respectively. P_2 involves about 3% error. Since $P_2 \ell_2$ contribution to $\int P(\ell) d\ell$ is less than 10 %, the 3% error in P_2 is reduced to less than

0.3% in the TCS.

3. Errors due to the inexact correction for thermal transpiration

The correction for P_1 possibly causes 0.8, 1.2, and 1.5% systematic error in the TCS for P_1 = 0.12, 0.06, and 0.04 Torr respectively. The correction for P_2 does not cause more than 0.2% error in the TCS.

4. Uncertainty of pressure distribution

First, the pressure gradient in the gas cell (excluding the vicinities of the exit apertures) should be carefully examined. Two out of the three measuring ports in the gas cell, located at the distance of 7 cm from the center of 20-cm-long gas cell, show 1 $\sim$ 2% lower pressure than the port located at the center. This, however, does not directly affect the accuracy of P_1' in Eq. (48). All the ports are connected to the sensor of the manometer with tubes of which the gas conductances are approximately same. During the TCS measurement, all the three ports are simultaneously opened. In this case the manometer reading is considered to be approximately the average pressure in the gas cell. The reading thus found is used as P_1' in Eq. (48), of which the error is expected to be appreciably reduced, $<$ 0.2 %.

Second, the pressure gradient out of the gas cell (excluding the vicinities of the apertures) is considered to

be the same order of magnitude as in the gas cell, and hence does not cause an error in the TCS more than a few tenth of percent.

Finally, the uncertainty around the exit apertures is most serious. The linear approximation, shown in Fig. 22, gives the exact value of $\int P(\ell)d\ell$, provided that the underestimate of gas pressure at one end of an aperture is cancelled out by the overestimate at the other end of the aperture. This is satisfied when the gas flow through the aperture is "molecular flow", and the gas flow entering the aperture has no extraordinary directivity. Present experimental condition is not far from above situation, because the mean-free-path of helium atoms in the used pressure is in the order of millimeter while the aperture diameter is 4 mm and the gas-cell diameter is 20 mm. The pressure is, however, slightly too high to be regarded entirely as "molecular flow", and there may possibly remain the error due to this approximation. As it is difficult to evaluate the error precisely, we consider here rather extreme case, where the pressure in the gas cell extends into the aperture by the depth equal to the aperture diameter. Then ℓ_1 = 22.4 (cm) and ℓ_2 = 13.8 (cm), and hence Eq. (48) underestimates the target thickness and overestimates the TCS by 2 %.

In conclusion, this value 2 % is considered to be a

reasonable upper limit of the total error due to the approximation for the pressure distribution.

5. Pressure dependence of the observed TCS

The measurement of TCS's with different pressure setting provides the means to examine several possible error sources. First, due to the large TCS's of impurities in the gas cell, the effect of them becomes significant at low pressure of helium gas, and results in an overestimate of e^+-He TCS's. Second, at a high pressure, multiple scattering may possibly become serious. This causes an underestimate of the TCS's. If the observed TCS's are consistent over the wide range of the pressure setting, it can be concluded that these two errors are negligible in the pressure used. In Fig. 23, we give the TCS's observed under different pressures. It can be seen all the TCS's for the same energy are in agreement within 2% differences. These plots also suggest that the systematic errors discussed in the preceding subsections act simply as a "scale factor" (not affected by the change of the pressure) to the TCS's.

B. Fluctuation of the Beam Intensity

Since we adopted the "segmentation, the long term variation of beam intensity, which mostly appears during several days after the installation of the moderator in the

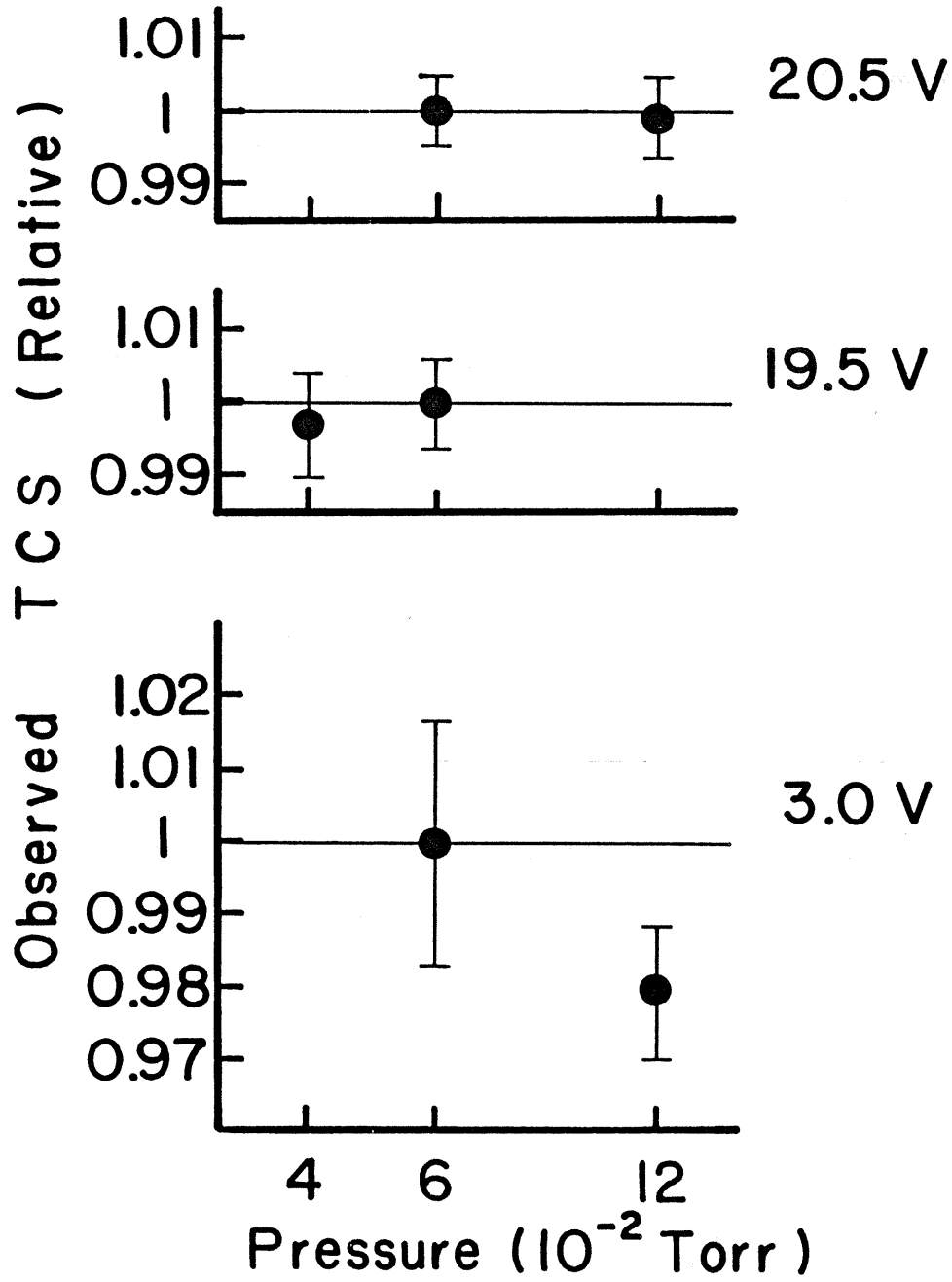

Fig. 23. Pressure dependence of observed TCS. Each TCS is derived with 2-eV bin width. Applied axial magnetic field is 8 G for 19.5-V run and 13 G for the others. The values at the left of the figure are accelerating voltages.

vacuum chamber, does not significantly affect the ratio n_v/n_g. The error due to the statistical fluctuation of beam intensity, denoted as $\Delta\sigma_{BI}$, is calculated by

$$\Delta\sigma_{BI} = \left(\int \rho(\ell)\, d\ell\right)^{-1} \sqrt{\left(\frac{\Delta n_v}{n_v}\right)^2 + \left(\frac{\Delta n_g}{n_g}\right)^2} \quad , \qquad (49)$$

where Δn_v and Δn_g are the statistical errors for the processed data n_v and n_g respectively.

For the energy-bin width of 0.2 or 0.5 eV, $\Delta\sigma_{BI}$ are 2 to 4 % above 3 eV and 4 to 10 % below 3 eV.

C. Forward Scattering

When the differential cross sections $\frac{d\sigma}{d\Omega}$ are given, the error in the TCS due to the incomplete discrimination against forward scattering, denoted as $\Delta\sigma_{FS}$, can be evaluated from

$$\Delta\sigma_{FS} = 2\pi \int_0^{\theta_m} \left(\frac{d\sigma}{d\Omega}\right) \sin\theta \, d\theta \quad , \qquad (50)$$

where θ_m is the discrimination angle, i.e., the maximum scattering angle of the positrons detected without colliding with the aperture wall. The angle θ_m in the uniform magnetic field can be estimated by the relation

$$\tan\theta_m = \frac{max.[v_2]}{v_1} = \frac{eBR}{mv_1} \quad , \qquad (51)$$

where e and m are the positron charge and mass, and v_1 and v_2 are the axial and transverse components of the velocity of a scattered positron, respectively. v_1 is approximately equal to the incident velocity. The max.[v_2] is the largest v_2 of scattered positrons detected without colliding with the wall, and is related to the product of the magnetic flux density B and the geometrically allowed maximum spiralling radius R for the scattered positrons. R depends on the distance between the scattering position and the spectrometer axis, but the reasonable choice of the effective R in the evaluation of $\Delta\sigma_{FS}$ is given by equating it to a half of the aperture radius (this value gives exact R if all the collisions occur on the axis), which is 1 mm for the present spectrometer.

The differential cross section can be calculated by the formula

$$\frac{d\sigma}{d\Omega} = |f(\theta)|^2$$

$$= k^{-2}\left|\sum_{L=0}^{\infty}(2L+1)[\exp(i\delta_L)](\sin\delta_L)P_L(\cos\theta)\right|^2 , \quad (52)$$

The error $\Delta\sigma_{FS}$ was calculated by the use of Eqs. (50)-(52) with a set of theoretical phaseshifts, i.e., δ_0 of Campeanu and Humberston (model H14),[14] δ_1 of Humberston and Campeanu (model H5),[16] δ_2 of McEachran et al.,[28] and δ_L ($3 \leq L \leq 10$) of the effective range formula by O'Malley et al.[17]

The results are shown in Fig. 24. For several values of BR, more rigorous calculation including up to 20th phaseshifts is carried out for the check of convergence. The difference of the results from those using up to 10th phaseshifts is found to be less than 0.3 % of the TCS's.

The errors $\Delta\sigma_{FS}$ are significantly large below about 3 eV, and rapidly decrease with the increase of energy. These curves are reffered in the last chapter to compare the present experimental results with the theory.

D. Spiralling of Incident Positrons

The spiralling of incident positrons due to the axial magnetic field causes two kinds of errors in the TCS's. One is introduced by the fact that the spiralling positrons have higher kinetic energies than the energy calculated from the flight time, as discussed in II-G. Therefore the observed TCS curve tends to shift toward the lower-energy side. This error becomes serious in the case where the true TCS varies rapidly with the increase of energy. As shown in II-G, the upper limit of energy shift is 0.15 eV for the axial magnetic field of 13 G and 0.06 eV for 8 G. Since the true energy shifts is several times smaller than the adopted energy-bin width, the error in the TCS's can be neglected as far as the TCS's presented in this thesis are regarded as the average value over the associated energy bin.

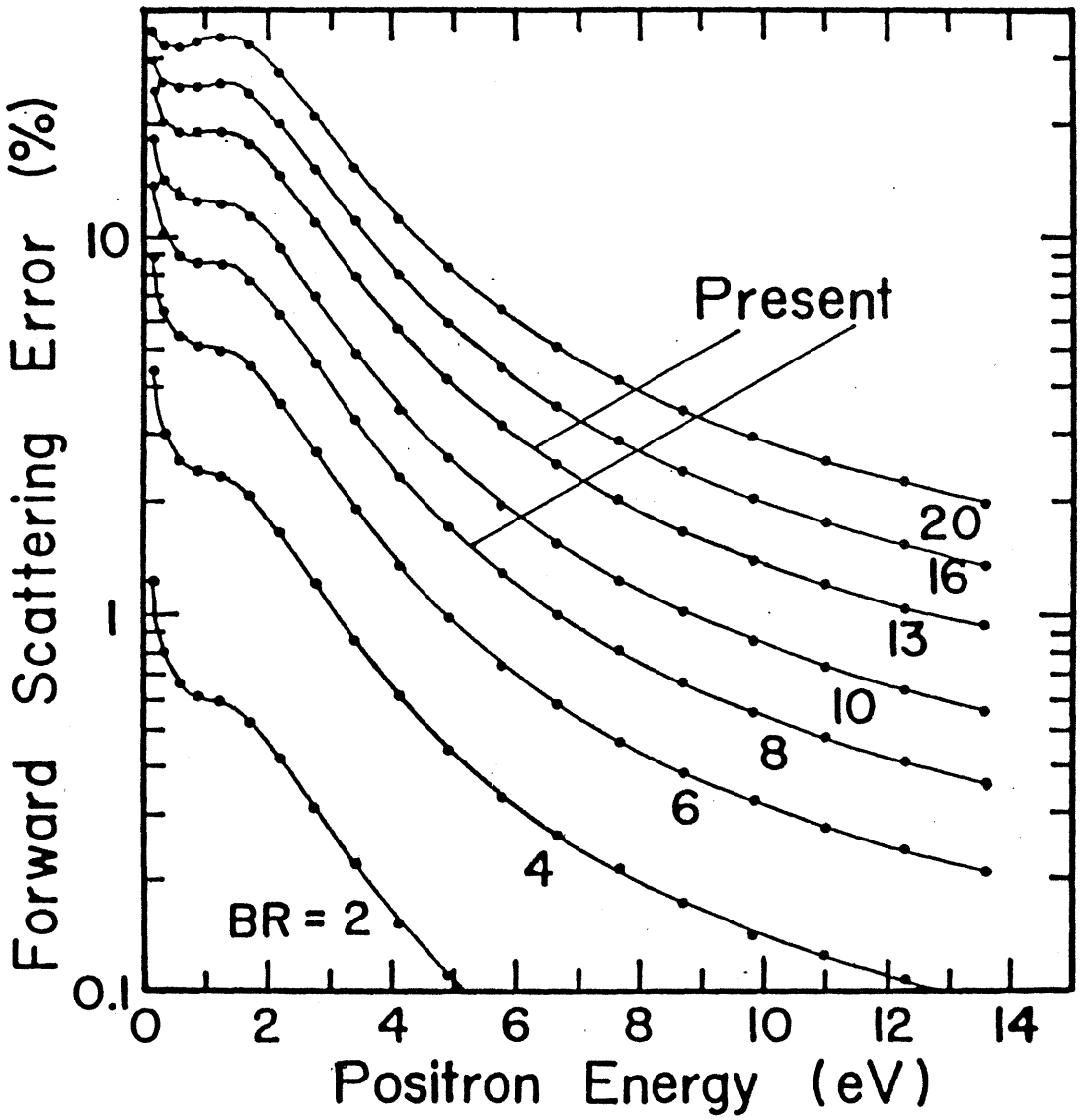

Fig. 24. Calculated forward scattering error. The numerical values of BR are given in G·mm.

The other error due to the spiralling comes from the fact that the spiralling positrons have the longer flight path in the gas cell than the geometrical gas-cell length. This causes some overestimate of the TCS's. We denote this error as $\Delta\sigma_{SP}$. The ratio of the excess length to the geometrical length is expressed for each positron as

$$\frac{\sqrt{v_1^2+v_2^2} - v_1}{v_1} = \sqrt{1+E_2/E_1} - 1 \ . \qquad (53)$$

where

$$E_1 = \frac{1}{2}mv_1^2 \ , \ E_2 = \frac{1}{2}mv_2^2 \ . \qquad (54)$$

Assuming the extreme angular distribution for incident positrons, where all the positrons are spiralling with the maximum allowed radius R, we can deduce the upper limit of the error $\Delta\sigma_{SP}$ by the use of Eq. (53) as

$$\begin{aligned} \Delta\sigma_{SP} &\simeq \sigma\cdot[\sqrt{1+\langle E_2\rangle/E_1} - 1] \\ &\simeq \sigma\cdot\frac{\langle E_2\rangle}{2E_1} \qquad (E_1 \rangle\rangle \langle E_2\rangle) \\ &< \sigma\cdot\frac{(eBR)^2}{4mE_1} \\ &\propto \sigma\cdot\frac{B^2}{E_1} \ . \end{aligned} \qquad (55)$$

For example, if E_1 = 2 eV and B = 13 G the upper limit is

4 %. The actual error $\Delta\sigma_{SP}$ is expected to be several times smaller than the upper limits.

E. Summary and Discussion

Among the statistical errors, $\Delta\sigma_{BI}$ are predominant, which are 2 to 4 % above 3 eV and amount to 10 % at the lowest measured energy 0.6 eV. The other factors, the manometer zero-drifts and the temperature drifts, amount to no more than 1 %. The systematic errors mainly consist of $\Delta\sigma_{FS}$, $\Delta\sigma_{SP}$, and a few percent scale-factor error due to the uncertainties of the pressure distribution and the thermal transpiration effects. Both $\Delta\sigma_{FS}$ and $\Delta\sigma_{SP}$ are significant only in low energy region. They tend to cancell each other, but the former is several times as large as the latter over the whole energy range. Note that both of them are related to the strength of axial magnetic field, and hence their magnitude can be experimentally estimated by comparing the observed TCS's in the different strengths of the magnetic field.

CHAPTER V

RESULTS AND DISCUSSION

The present results of positron-helium total cross sections (TCS's) for two different settings of the axial magnetic field are tabulated in Tables 2 and 3. In this chapter we compare our results to the previous experimental and theoretical TCS's by other groups.

A. Below the Ps-Formation Threshold

1. Theoretical background

Only the elastic scattering can occur in the energy range below the positronium (Ps) formation threshold 17.8 eV. The TCS can be expressed as a sum of partial-wave contributions.

$$\sigma = \frac{4\pi}{k^2} \sum_{L=0}^{\infty} (2L+1) \sin^2 \delta_L \quad , \qquad (56)$$

where k is a wave number of the incident positrons, and δ_L is the phaseshifts of the L-th partial wave.

Theoretical calculations of the phaseshifts were performed by many groups. The Kohn variational method was applied to calculate s-[13,14] and p-wave[15,16] phaseshifts. The optical potential method was used for s-wave calculation.[29] Provided an exact wavefunction of the target

Table 2. e^+-He total cross sections with statistical uncertainties measured in 8 G axial magnetic field. The boundaries of energy-bins are listed in the left columns.

Energy (eV)	TCS (πa_0^2)	Energy (eV)	TCS (πa_0^2)
0.5- 0.7	0.135 ± 0.015	17.1-17.3	0.233 ± 0.006
0.7- 0.9	0.101 ± 0.009	17.3-17.5	0.233 ± 0.006
0.9- 1.1	0.094 ± 0.008	17.5-17.7	0.236 ± 0.006
1.1- 1.3	0.081 ± 0.007	17.7-17.9	0.252 ± 0.006
1.3- 1.5	0.085 ± 0.005	17.9-18.1	0.249 ± 0.006
1.5- 1.7	0.075 ± 0.005	18.1-18.3	0.251 ± 0.006
1.7- 1.9	0.070 ± 0.006	18.3-18.5	0.256 ± 0.006
1.9- 2.1	0.070 ± 0.006	18.5-18.7	0.263 ± 0.006
2.1- 2.3	0.067 ± 0.006	18.7-18.9	0.277 ± 0.007
2.3- 2.5	0.077 ± 0.006	18.9-19.1	0.281 ± 0.007
2.5- 2.7	0.081 ± 0.006	19.1-19.3	0.289 ± 0.007
		19.3-19.5	0.293 ± 0.007
15.1-15.3	0.237 ± 0.007	19.5-19.7	0.300 ± 0.006
15.3-15.5	0.226 ± 0.007	19.7-19.9	0.311 ± 0.006
15.5-15.7	0.223 ± 0.007	19.9-20.1	0.311 ± 0.006
15.7-15.9	0.227 ± 0.007	20.1-20.3	0.320 ± 0.006
15.9-16.1	0.230 ± 0.007	20.3-20.5	0.326 ± 0.006
16.1-16.3	0.225 ± 0.006	20.5-20.7	0.331 ± 0.007
16.3-16.5	0.235 ± 0.006	20.7-20.9	0.344 ± 0.009
16.5-16.7	0.237 ± 0.006	20.9-21.1	0.353 ± 0.009
16.7-16.9	0.233 ± 0.005	21.1-21.3	0.362 ± 0.009
16.9-17.1	0.234 ± 0.005	21.3-21.5	0.368 ± 0.009
		21.5-21.7	0.362 ± 0.010

Table 3. e^+-He total cross sections with statistical uncertainties measured in 13 G axial magnetic field. The boundaries of energy-bins are listed in the left columns.

Energy (eV)	TCS (πa_0^2)	Energy (eV)	TCS (πa_0^2)
0.5 - 0.7	0.127 ± 0.008	10.25-10.75	0.203 ± 0.008
0.7 - 0.9	0.090 ± 0.007	10.75-11.25	0.202 ± 0.007
0.9 - 1.1	0.085 ± 0.006	11.25-11.75	0.213 ± 0.007
1.1 - 1.3	0.076 ± 0.005	11.75-12.25	0.213 ± 0.007
1.3 - 1.5	0.067 ± 0.004		
1.5 - 1.7	0.063 ± 0.004	13.25-13.75	0.219 ± 0.006
1.7 - 1.9	0.066 ± 0.004	13.75-14.25	0.224 ± 0.006
1.9 - 2.1	0.070 ± 0.004	14.25-14.75	0.221 ± 0.006
2.1 - 2.3	0.067 ± 0.004	14.75-15.25	0.228 ± 0.006
2.3 - 2.5	0.081 ± 0.005	15.25-15.75	0.233 ± 0.006
2.5 - 2.7	0.079 ± 0.004	15.75-16.25	0.229 ± 0.006
2.7 - 2.9	0.077 ± 0.004	16.25-16.75	0.229 ± 0.005
2.9 - 3.1	0.083 ± 0.005	16.75-17.25	0.232 ± 0.005
		17.25-17.75	0.246 ± 0.007
3.25- 3.75	0.102 ± 0.003	17.75-18.25	0.245 ± 0.006
3.75- 4.25	0.113 ± 0.003	18.25-18.75	0.263 ± 0.006
4.25- 4.75	0.121 ± 0.003	18.75-19.25	0.276 ± 0.006
4.75- 5.25	0.126 ± 0.004	19.25-19.75	0.293 ± 0.007
5.25- 5.75	0.137 ± 0.005	19.75-20.25	0.319 ± 0.008
5.75- 6.25	0.147 ± 0.005	20.25-20.75	0.326 ± 0.007
		20.75-21.25	0.365 ± 0.008
7.25- 7.75	0.166 ± 0.006	21.25-21.75	0.375 ± 0.008
7.75- 8.25	0.173 ± 0.006	21.75-22.25	0.391 ± 0.009
8.25- 8.75	0.181 ± 0.006		
8.75- 9.25	0.188 ± 0.006		

atom is known, these two methods satisfy the "bound theorems".[30,31] Therefore, these methods are expected to be more effective than the other approximate theories. The former method gives an upper bound[30] of the exact scattering length a, i.e.,

$$a = \lim_{k \to 0} \frac{-\tan \delta_0}{k} \qquad (57)$$

while the latter method gives an lower bound[31] of the exact phaseshift as well as an upper bound of a. Since, unfortunately, the exact wavefunction is not known except for a hydrogen atom, the bound principles are not valid in an exact sence. To overcome this difficulty, the "Method of Models"[32] is adopted,[13-16,29] i.e., the exact target hamiltonian is replaced by the "model" hamiltonian, which makes the adopted approximate wavefunction of the atom concerned equal to the exact eigenfunction. Thus the bound principles are "restored", within the reliability of the adopted "model". In Refs. 13-16, the accuracy of the target function was systematically improved (model DB → model H5 → model H14), and well-converged phaseshifts were obtained. Their methods are theoretically sound, and the results seems to be most reliable today. The optical potential method[29] is also theoretically sound, but the atomic wavefunction used is less accurate. For 0-th to 3rd phaseshifts, another variational calculation by the Kohn-Hulthen method was

performed by Aulenkamp et al.[33] Their trial functions are less flexible, and their results are far from those of the other calculations.

The other theoretical works more or less contain a priori assumptions to simplify the original Schrödinger equation. Their advantage is the applicability to the case of the more complex target atoms than helium, although validity of the theories should be examined by using more rigorous theories or, from an essential point of view, by using precise experimental data. "Polarized orbital" approximation was applied to positron-helium scattering by McEachran et al.[28] to calculate 0 to 6th phaseshifts, and by Drachman[34] to calculate s-, p-, and d-wave phaseshifts. Amusia et al.[35] used the "random phase approximation with exchange" to calculate 0 to 3rd phaseshifts. Schrader[36] developed a simple semi-empirical polarization potential method which contains a disposable parameter called "effective radius".

For the partial waves other than s-wave, k-expansion of the phaseshifts for the scattering of a charged particle by a neutral polarizable target, presented by O'Malley et al.,[17] may be applicable in some energy range.

$$\delta_L = \frac{\pi P k^2}{(2L-1)(2L+1)(2L+3)} + \begin{cases} O(k^3) & (\text{for } L=1) \\ O(k^4) & (\text{for } L>1) \end{cases}, \qquad (58)$$

where P is the dipole polarizability of the target atom.

Theoretical results for s-, p-, and d-wave phaseshifts are summarized in Figs. 25, 26, and 27, respectively. It can be seen in Fig. 25 that the result of Ho and Fraser (model HF2) is more positive than that of Campeanu and Humberston (model H14 or H5), although the former gives lower bound of the phaseshift within the reliability of the adopted target wavefunction. As the target wavefunction of the latter is more accurate than that of the former, a bound calculation like the former with more accurate target function may be required to obtain further definite s-wave phaseshift. The p-wave phaseshifts of Humberston and Campeanu (model H5),[16] Amusia et al., and McEachran et al. are in good agreement in the range of $k < 0.7$ (especially the latter two are in good agreement over the whole calculated range). For d-wave, it can be seen that the curve of O'Malley et al. goes close to the results of the more elaborate calculations with the decrease of k.

2. Results around the Ramsauer minimum

In Figs. 28 and 29, the present results below 6 eV are compared to the other experimental and theoretical TCS's. Obviously both sets of the present results (obtained in 8 and 13 G axial magnetic field) are higher than those of Stein et al.[8] except for the range below 1 eV, and are rather in good agreement with the results of Wilson[11,12] and of Canter et al.[9] Our measurements in 8 G magnetic field give

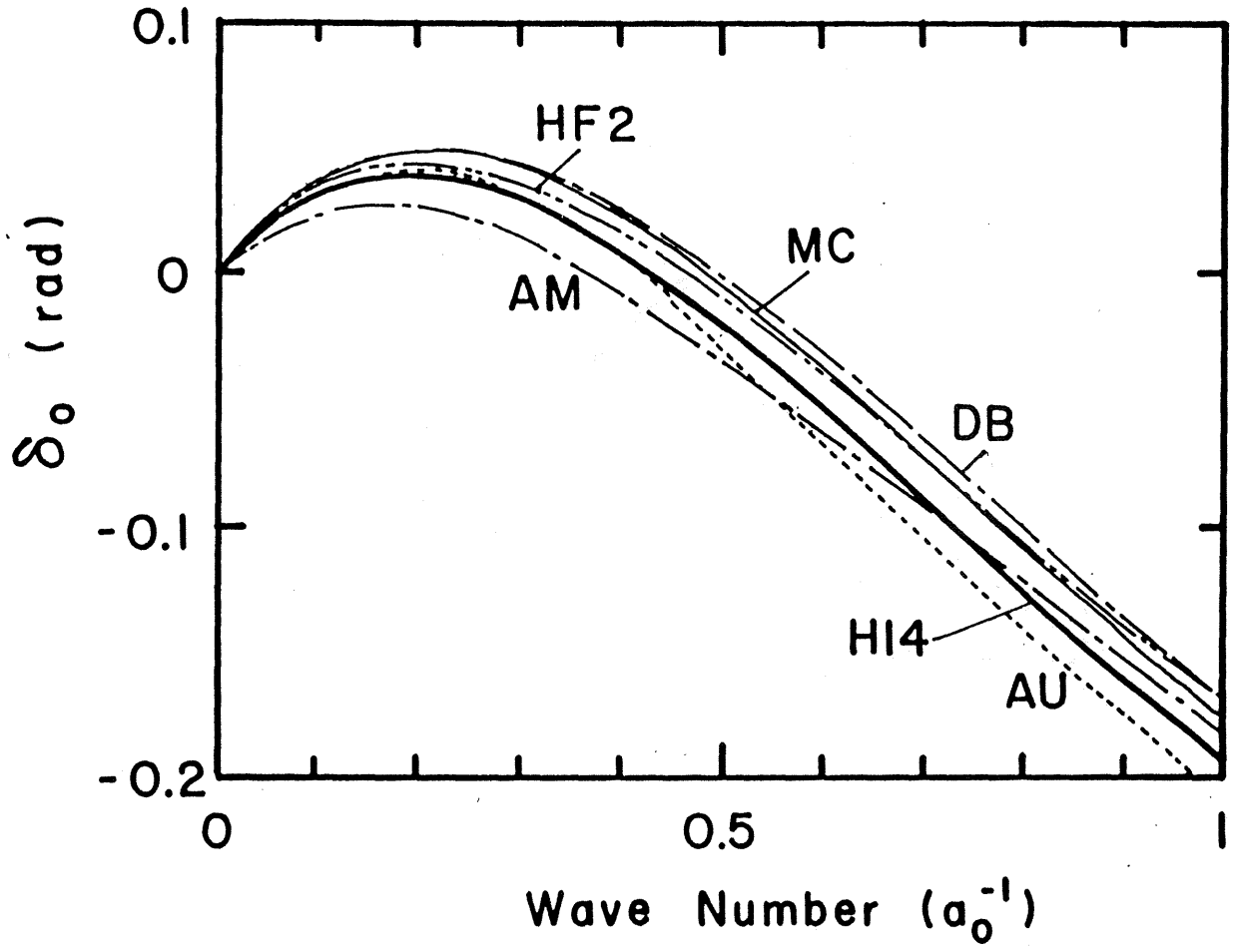

Fig. 25. *s*-wave phaseshifts. H14, Ref. 14 (model H14); DB, Ref. 13 (model DB); HF2, Ref. 29 (model HF2); MC, Ref. 28; AM, Ref. 35; AU, Ref. 33. The results by model H5 (Ref. 13) are close to the curve H14, and are not drawn in this figure for clarity.

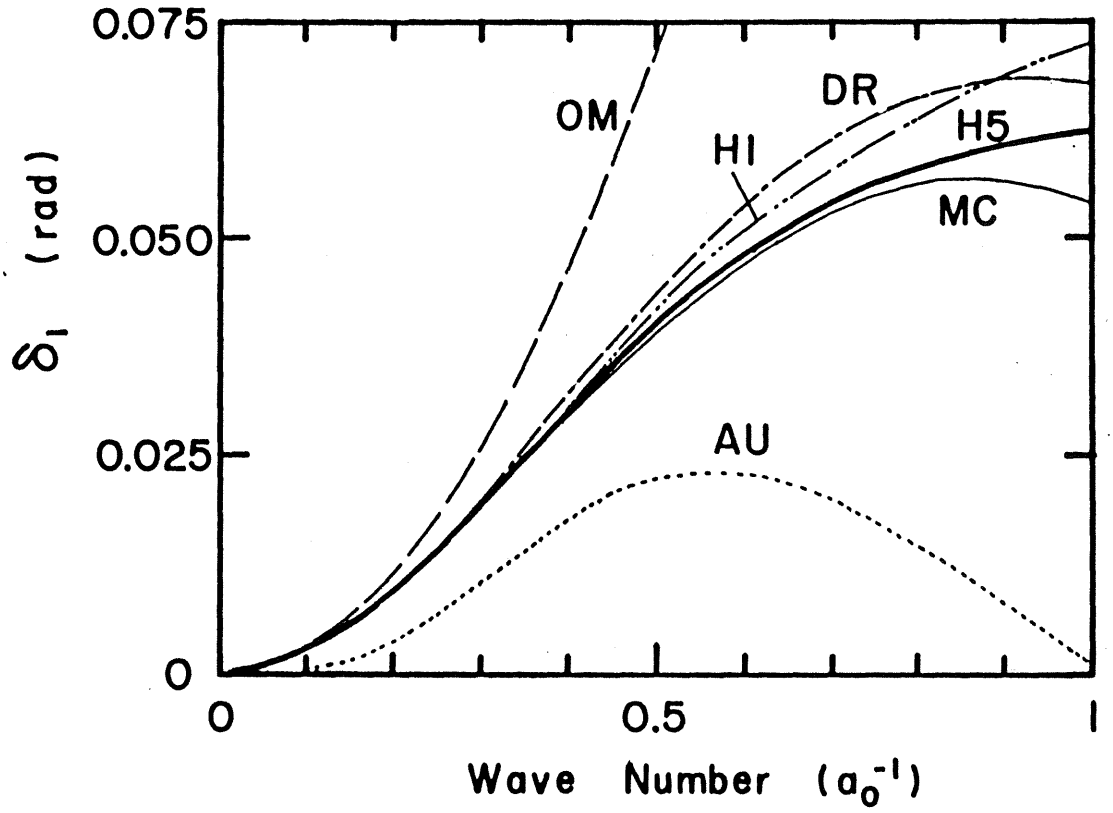

Fig. 26. *p*-wave phaseshifts. H5, Ref. 16 (model H5); H1, Ref. 16 (model H1); MC, Ref. 28; DR, Ref. 34; AU, Ref. 33; OM, Ref. 17. The results of Ref. 35 (Amusia et al.) are close to the curve MC, and are not drawn in this figure.

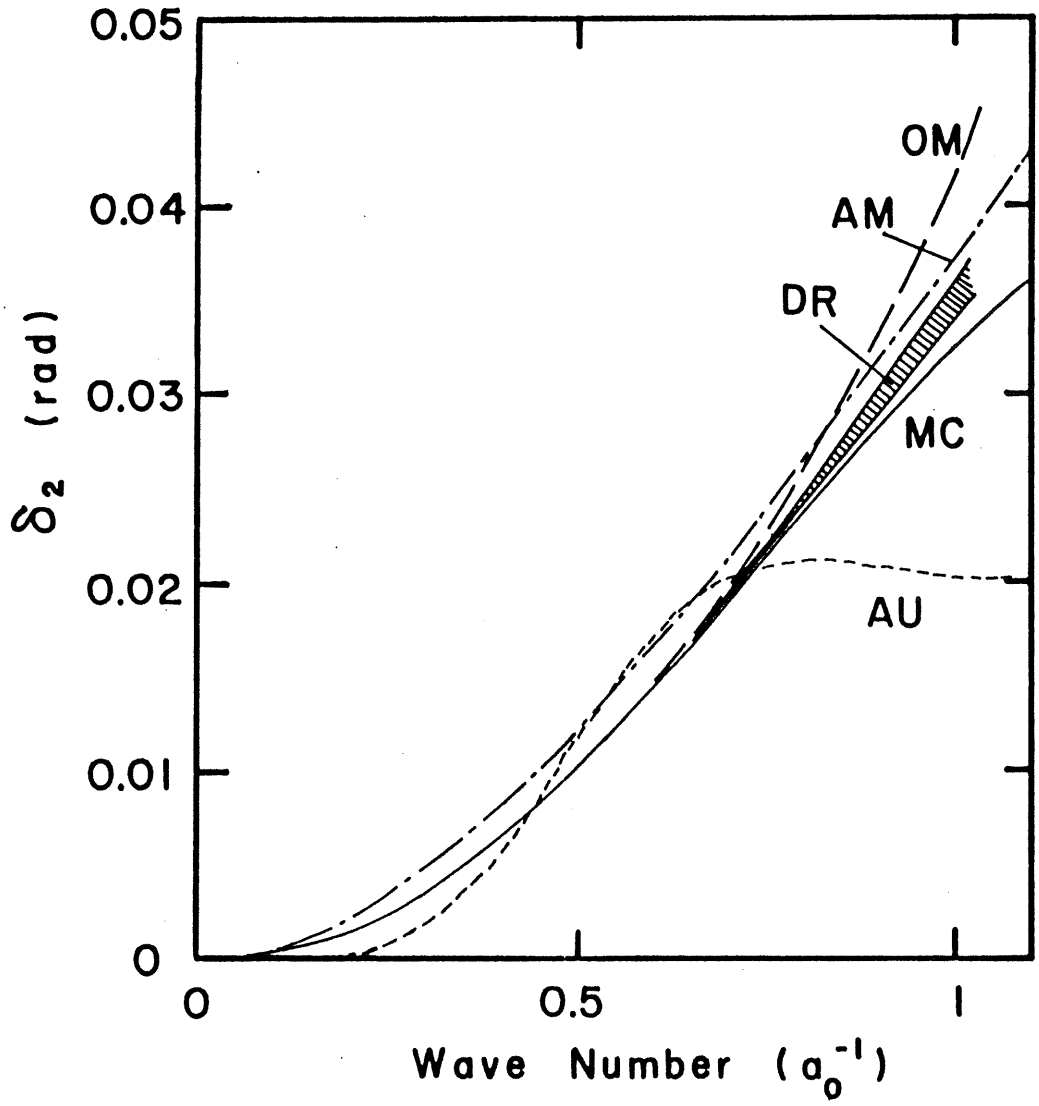

Fig. 27. *d*-wave phaseshifts. MC, Ref. 28; AM, Ref. 35; DR, Ref. 34; AU, Ref. 33; OM, Ref. 17.

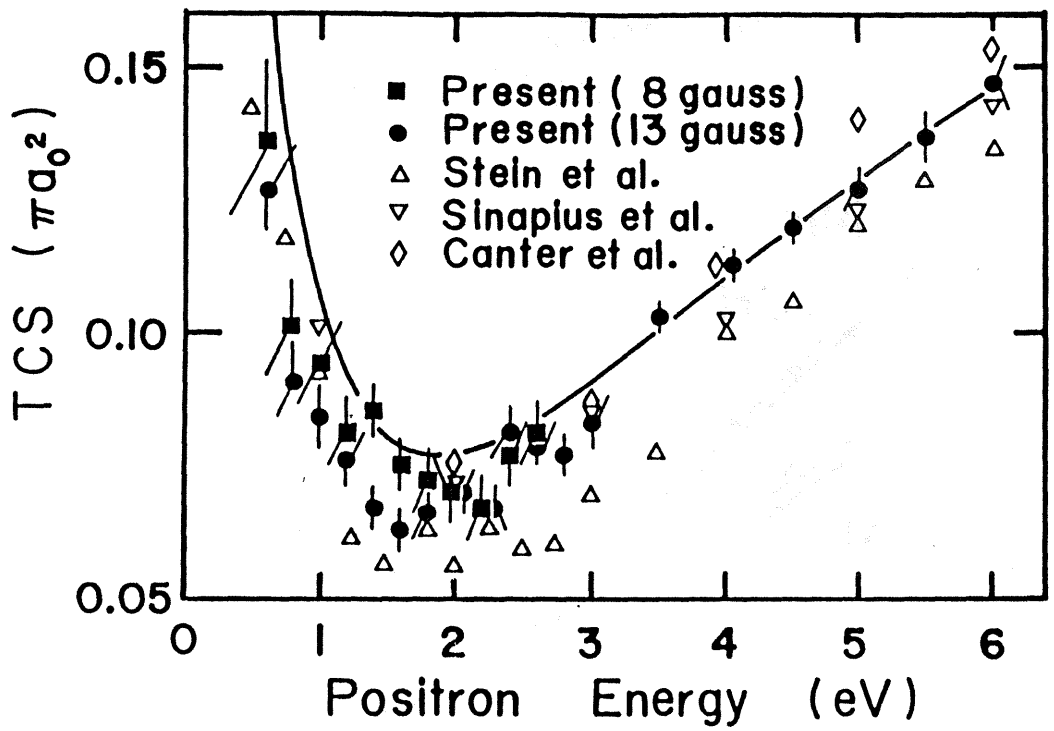

Fig. 28. Present results for positron-helium total cross sections around the Ramsauer minimum. Quoted results are from Ref. 8 (Stein et al.), Ref. 9 (Canter et al.), and Ref. 12 (Sinapius et al.). Solid curve represents theoretical results deduced from δ_0 (Ref. 14), δ_1 (Ref. 16, model H5), and higher partial waves of Ref. 17.

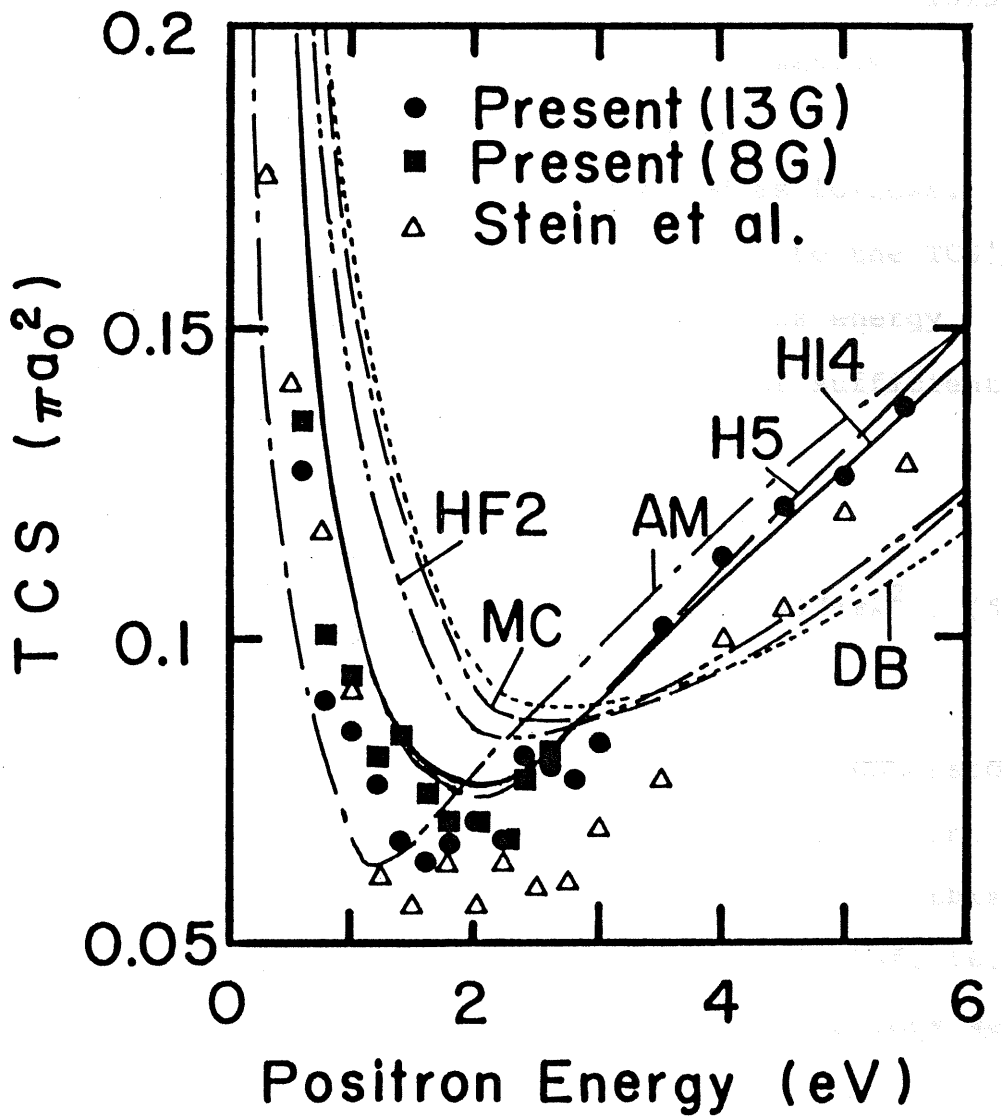

Fig. 29. Comparison of the present results to various theoretical results in the vicinity of the Ramsauer minimum. δ_1 of Ref. 16 (model H5) and δ_L ($L > 1$) of Ref. 17 are used for all the curves. δ_0 is taken from Ref. 14 (H14), Ref. 13 (H5), Ref. 13 (DB), Ref. 28 (MC), Ref. 35 (AM), and Ref. 29 (HF2).

systematically larger values than those of 13-G runs. This fact suggests better discrimination against forwardly-scattered positrons in the weaker-field runs.

Theoretical curves in Fig. 29 are deduced as follows. The contribution of the phaseshifts above $L = 2$ to the TCS's is no more than a few percents altogether in this energy range, and the use of O'Malley's formula[17] gives sufficiently accurate estimate of this contribution,

$$\frac{4\pi}{k^2} \sum_{L=2}^{\infty} (2L+1) \sin^2 \left[\frac{\pi P k^2}{(2L-1)(2L+1)(2L+3)} \right] = 0.04177 \pi k^2 \quad , \quad (59)$$

where $P = 1.38\ (a_0{}^2)$. For p-wave, the results of Humberston and Campeanu (model H5)[16] was used, which are in agreement with those of McEachran et al. and of Amusia et al. in this energy range within the uncertainties presented in Ref. 16. Finally, only for s-wave, several different calculations were examined.

As seen in Fig. 29, appreciable discrepancies exist among the resultant theoretical TCS's, while the present results clearly resolve the ambiguity. The minimum in Amusia's results is too deep and energetically too low, and those of McEachran et al. and of Ho and Fraser are too shallow and too high. The results of Kohn methods with the model H5 and the model H14 give best agreement with the present results,

although slight discrepancy remains. This discrepancy can be fully explained, however, by taking account for the error due to forward scattering. We estimated the error $\Delta\sigma_{FS}$ in CHAPTER IV, and the resultant $\Delta\sigma_{FS}$ is depicted in Fig. 24. By adding $\Delta\sigma_{FS}$ to the observed TCS's, we obtain the TCS's corrected for forward scattering error (see Fig. 30). Both sets of the corrected TCS's, for 8 G and 13 G runs, are in further better agreement with the results of the Kohn methods quoted above. Furthermore, after the correction, the difference between two sets of the present results has disappeared within the statistical uncertainties. This suggests that another systematic error, $\Delta\sigma_{SP}$, is not significant. The other systematic error due to the uncertainty of the gas density distribution is estimated to be no more than a few percents. Therefore, in this energy range, we can conclude that the Kohn methods with the model H5 or H14 gives accurate TCS's within the present statistical uncertainties of several percents.

3. Results at higher energies

The present results in the energy range below the Ps-formation threshold are shown in Fig. 31. Above about 7 eV they are in agreement with the results of Stein et al.[8] within the statistical uncertainties, although the present ones seem to be a few percent higher systematically. The data of Canter et al.[9] seem to be 6-7% lower than the present

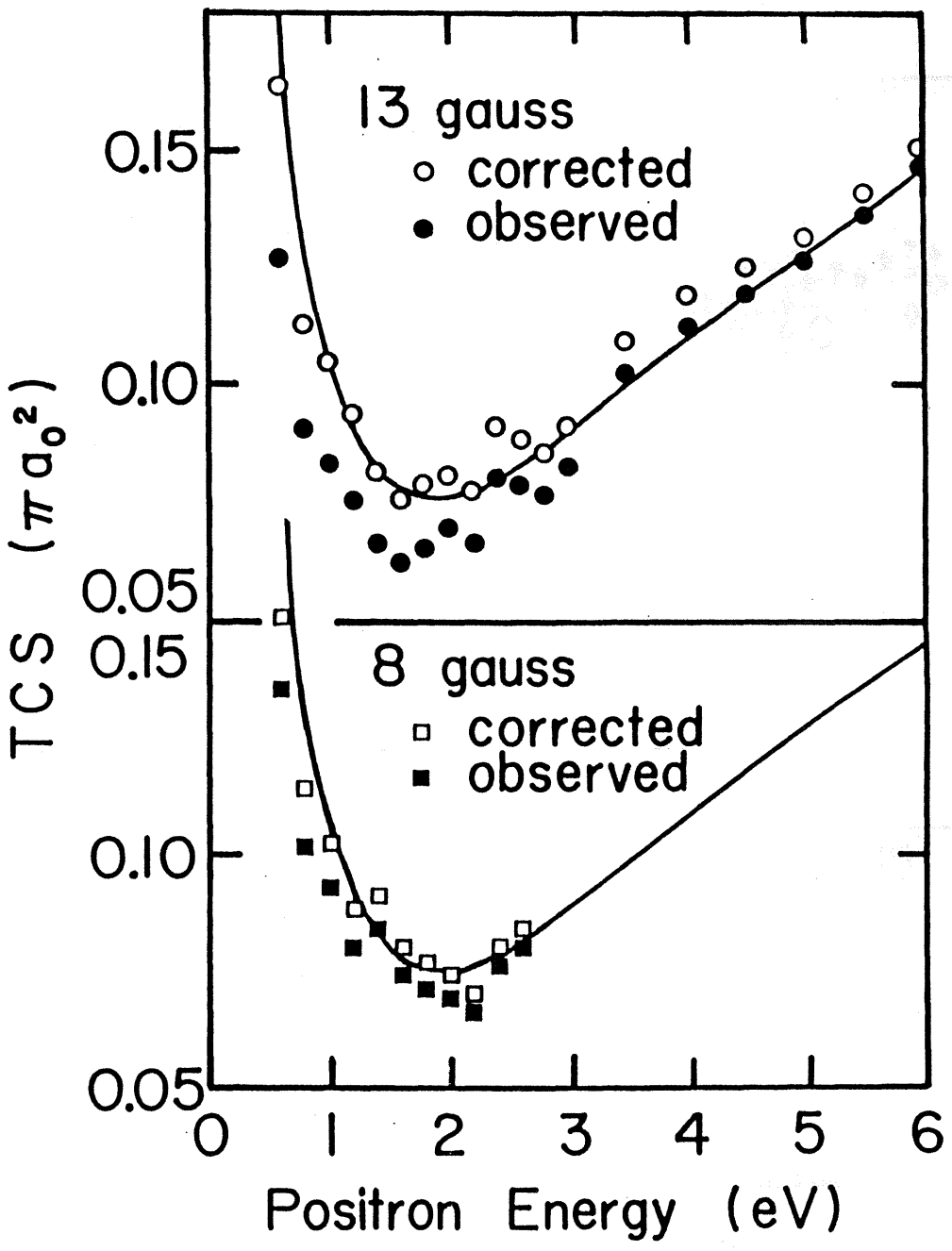

Fig. 30. Comparison of the theoretical results to the present results with and without correction for the forward scattering errors. Solid curve is the same as that of Figs. 28 and 29.

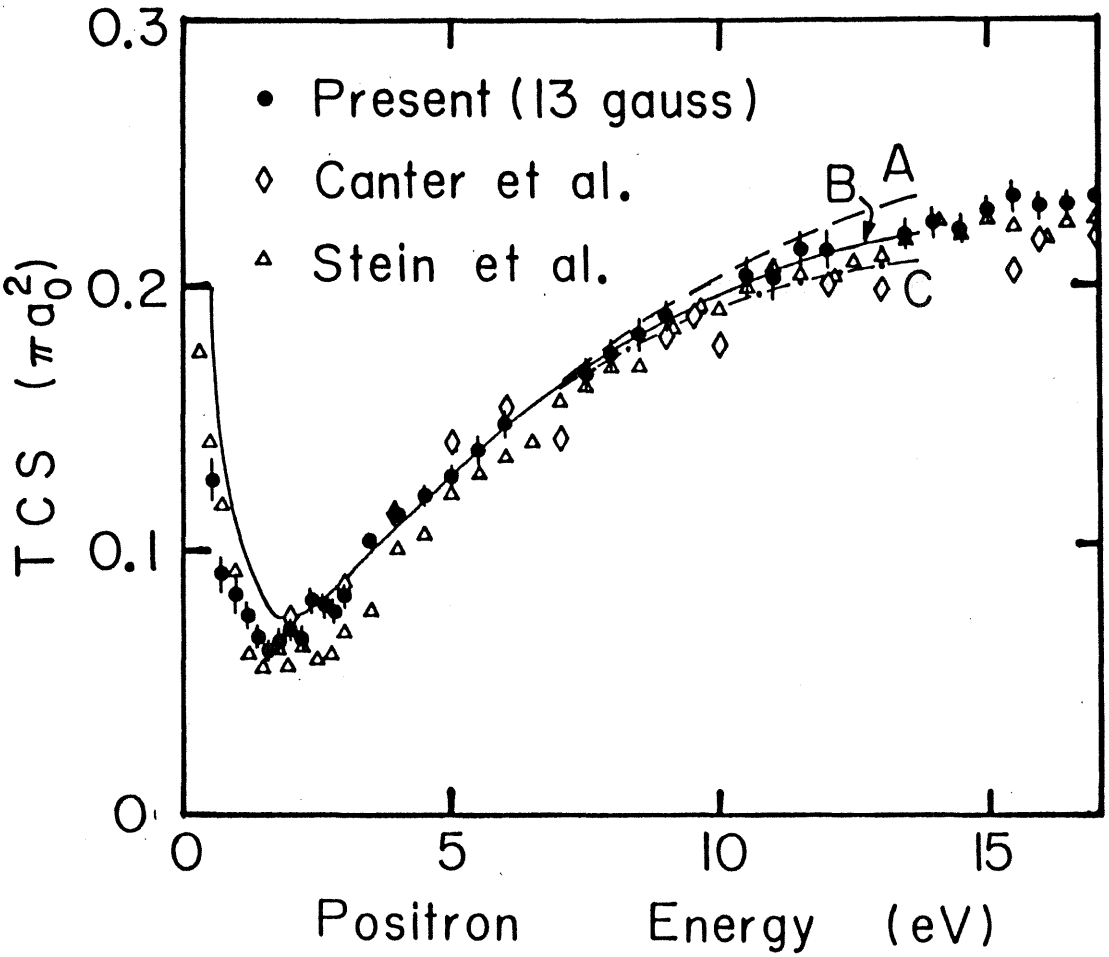

Fig. 31. Present results for positron-helium total cross sections below the Ps-formation threshold. Quoted experimental results are taken from Ref. 8 (Stein et al.) and Ref. 9 (Canter et al.) The curves are explained in the text.

ones on the average. In this region the systematic error in the present data is dominated by a few percent scale-factor error due to the uncertainty of the gas density distribution ($\Delta\sigma_{FS}$ and $\Delta\sigma_{SP}$ are small enough, see CHAPTER IV), and therefore the difference from the data of Canter et al. is meaningfull, while the difference from the data of Stein et al. is not significant.

Comparison to the theories is made as follows. First, for s-wave, it has been shown in the previous subsection that the phaseshift by the Kohn variational method[13,14] with the model H5 or H14 is most reliable, and here we adopt the results by the model H14 (the use of model H5 will raise the resultant TCS's by no more than 2 % at 13.6 eV). Second, the choice of p- and d-wave phaseshifts causes appreciable differences in the TCS's in this region. For p-wave, the variational results by the model H5,[16] the results of McEachran et al.,[28] and the results of Amusia et al.[35] seem to be most reliable, for they are in good agreement in the range below k = 0.7 (6.7 eV). The latter two agree over the whole calculated range, and go lower above k = 0.7 than the results of H5. Therefore we examine two sets of p-wave phaseshifts, i.e., the model H5 and the McEachran's. For d-wave, four different sets of phaseshifts, i.e., by O'Malley et al., Amusia et al., Drachman[34], and McEachran et al., are examined. The contribution of the higher partial waves are

evaluated by using O'Malley's formula.

$$\frac{4\pi}{k^2}\sum_{L=3}^{\infty}(2L+1)\sin^2\left[\frac{\pi P k^2}{(2L-1)(2L+1)(2L+3)}\right] = 0.00767\pi k^2 \quad , \quad (60)$$

where we assigned $P = 1.38\ (a_0^2)$.

In Fig. 31 the theoretical TCS's obtained from three combinations of the phaseshifts are shown, i.e.,

Curve A: s(H14), p(H5), d(O'Malley)

Curve B: s(H14), p(H5), d(McEachran)

Curve C: s(H14), p(McEachran), d(McEachran).

The resultant curves by using the other combinations are distributing among these three curves. For example, substituting *d*-wave phaseshifts in the curve B by Drachman's or Amusia's, the resultant curve is raised by 2 % or 3 % at 13.6 eV, respectively.

The present experimental results are in excellent agreement with the curve B. The curve A is 6% higher, and the curve C is 5% lower at 13.6 eV than the curve B. These differences are somewhat larger than the systematic errors in the present measurements. Therefore we conclude that the curve B gives accurate TCS's with a few % error.

Most of the previous experimental data are distributing between the curve B and C. Therefore, even if there exists any unresolved errors in the present measurements, we believe the overall error does not exceed several percents. This

provides another support for the reliability of the present results in the lower energy region, i.e., around the Ramsauer minimum.

B. Around and Above the Ps-Formation Threshold

The present results above 15 eV are shown in Fig. 32. Two sets of the obtained TCS's, measured in two different strengths of the axial magnetic field, are in good agreement in this region. Therefore it can be concluded that both sets are free from the forward scattering error and the spiralling error. Remaining systematic error is estimated to be no more than a few percents. The results are also in fairly good agreement with the experimental results of the other groups.[8-10]

It can be seen that the rapid increase of the TCS starts at the Ps-formation threshold due to the opening of a new channel, i.e., the Ps formation, as previously observed by other groups. In the previous data by the other groups, the onsets of the increase are rather obscure, and seem to be located lower than the exact threshold 17.8 eV by several tenths of eV. This suggests the existence of small error in their energy determination. On the other hand, the onset in the present data is clearly located at $\sim$17.7 eV. As our energy determination slightly underestimates true energies

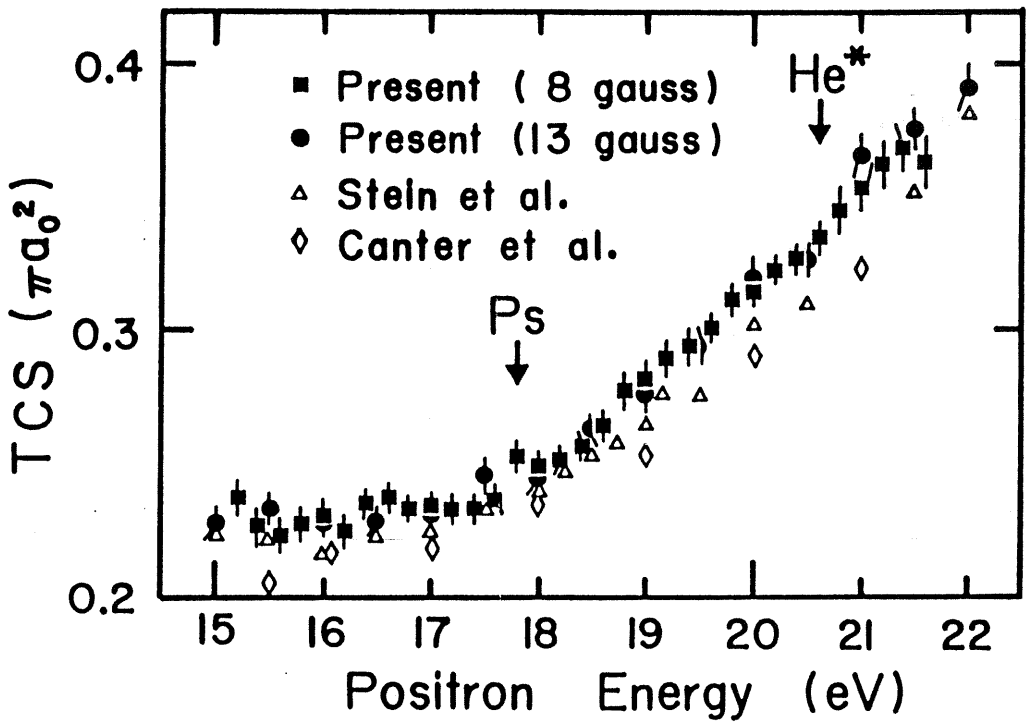

Fig. 32. Present results for positron-helium total cross sections around the Ps-formation threshold. Quoted results are taken from Ref. 8 (Stein et al.) and Ref. 9 (Canter et al.)

(not more than 0.2 eV, see II-G-3), we can conclude that really discontinuous change of the slope occur at the Ps-formation threshold. This phenomenon may provide one of standards of energy calibration for future positron scattering experiments.

In the energy region from the Ps-formation threshold to the first atomic excitation threshold ($He(2^1S)$, 20.6 eV), called "Ore gap", two scattering channels are open: the elastic scattering and the Ps formation. Theories required in this region should give two partial cross sections which correspond to the two channels, with the accuracy comparable to that of the experimental TCS's. Moreover, as positron-helium scattering is the simplest case where theoretical results can be compared to experimental data today, the theories should be preferably "rigorous" to some extent, like the Kohn method with "method of models" in the single channel case. Once the results of "rigorous" calculations become consistent with the accurate experimental TCS's for the positron-helium case, they can be used as a reliable standard for checking any experimental methods and simpler approximate theories to study more complex cases. Unfortunately no such a calculation exists so far. However several attempts to calculate the Ps-formation cross sections in positron-helium scattering were performed[37-42] by the methods of which the validities are not known. Here we compare the present

results to the calculations in the following rather indirect way.

The Ps-formation cross sections are estimated from the present TCS data as follows. The TCS curve below the threshold, where only elastic scattering can occur, is smoothly extrapolated beyond the threshold, and is subtracted from the measured TCS's above the threshold. Then the remainder is expected to represent the Ps-formation cross section. This smooth extrapolation is partly supported for positron-hidrogen s-wave case, by a two-channel variational calculation.[43] In general, however, there exists no evidence to confirm this procedure. The slope of elastic cross section should tend to decrease, in principle, when the impact energy is raised through an inelastic scattering threshold. Hence the results of above procedure should be considered as lower estimates of the exact Ps-formation cross sections. In Fig. 33, such results are compared to the recent two theoretical results,[41,42] as well as other experimental data. The results of the extrapolation procedure by other groups (not plotted in the figure) are in fairly good agreement with the present ones, as expected from the agreement among the observed TCS's. The results of direct measurements for the Ps-formation by Charlton et al.[4] are somewhat lower. They are in serious disagreement with the other direct measurements by Fornari et al.[5] over the

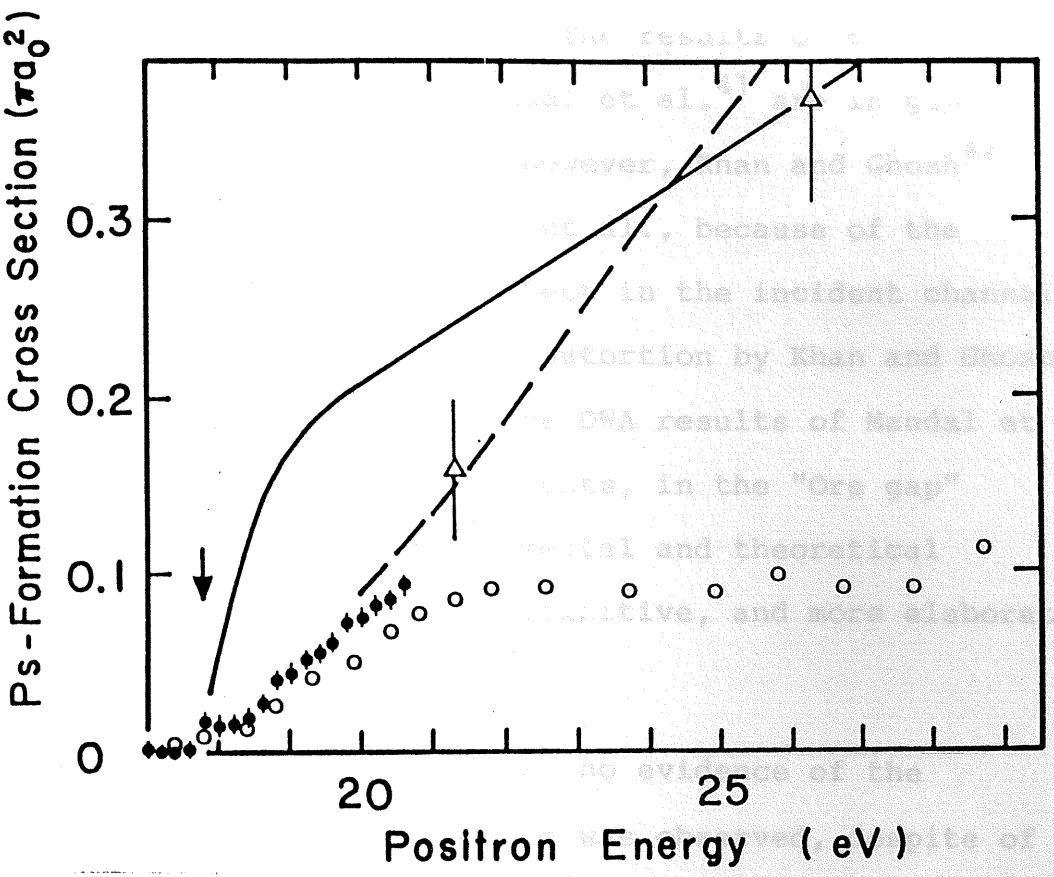

Fig. 33. Positronium-formation cross sections. Closed circle, present estimate; open circle, Ref. 4; triangle, Ref. 5; solid curve, Ref. 42; dashed curve, Ref. 41. The arrow indicates the location of the Ps-formation threshold.

whole overlapped energy region. The results of distorted wave approximation (DWA) by Mandal et al.[41] are in good agreement with Fornari et al. However, Khan and Ghosh[42] criticized the method of Mandal et al., because of the neglect of target distortion effect in the incident channel. The results of DWA with target distortion by Khan and Ghosh[42] are several times larger than the DWA results of Mandal et al. and all the experimental results, in the "Ore gap" region. Therefore, both experimental and theoretical situations are still far from definitive, and more elaborate works are required.

Finally, in the present data, no evidence of the resonance below the 2^1S threshold was observed, despite of the suggestion by Ho and Fraser.[29] Definite conclusion is, however, still impossible because of the limited energy resolution and the statistical uncertainties. Further investigation with the improved apparatus is in progress.

C. Conclusions

Reliable experimental TCS's of positron-helium scattering were obtained with several percent errors over the energy range from 0.6 eV to 22 eV. The ambiguity among the previous experimental TCS's around the Ramsauer minimum was clearly resolved, and it has been confirmed that the s- and p-wave

phaseshifts by the Kohn variational methods with "method of models" give accurate TCS's over the whole calculated range. The results around the Ps-formation threshold were consistent with those of the other groups within several percent uncertainties. In this region the experimental TCS's seem to be well-established, and reliable theoretical calculations on this two-channel probrem are expected.

REFERENCES

1. C. J. Crannel, G. Joyce, R. Ramaty, and C. Werntz, Astrophys. J. 210, 582 (1976); M. Leventhal, C. J. MacCallum, and P. D. Stang, Astrophys. J. 225, L11 (1978).
2. D. G. Costello, D. E. Groce, D. F. Herring, and J. Wm. McGowan, Can. J. Phys. 50, 23 (1972).
3. A comprehensive review on the subject is given in: W. E. Kauppila and T. S. Stein, Can. J. Phys. 60, 471 (1982).
4. M. Charlton, G. Clark, T. C. Griffith, and G. R. Heyland, J. Phys. B 16, L465 (1983).
5. L. S. Fornari, L. M. Diana, and P. G. Coleman, Phys. Rev. Lett. 51, 2276 (1983).
6. P. G. Coleman and J. D. McNutt, Phys. Rev. Lett. 42, 1130 (1979).
7. P. G. Coleman and J. T. Hutton, Phys. Rev. Lett. 45, 2017 (1980).
8. T. S. Stein, W. E. Kauppila, V. Pol, J. H. Smart, and G. Jesion, Phys. Rev. A 17, 1600 (1978).
9. K. F. Canter, P. G. Coleman, T. C. Griffith, and G. R. Heyland, J. Phys. B 6, L201 (1973).
10. J. R. Burciaga, P. G. Coleman, L. M. Diana, and J. D. McNutt, J. Phys. B 10, L569 (1977).
11. W. G. Wilson, J. Phys. B 11, L629 (1978).
12. G. Sinapius, W. Raith, and W. G. Wilson, J. Phys. B 13,

4079 (1980).

13. J. W. Humberston, J. Phys. B 6, L305 (1973).
14. R. I. Campeanu and J. W. Humberston, J. Phys. B 10, L153 (1977).
15. R. I. Campeanu and J. W. Humberston, J. Phys. B 8, L244 (1975).
16. J. W. Humberston and R. I. Campeanu, J. Phys. B 13, 4907 (1980).
17. T. F. O'Malley, L. Rosenberg, and L. Spruch, Phys. Rev. 125, 1300 (1962).
18. J. W. Humberston, J. Phys. B 11, L343 (1978).
19. J. M. Wadehra, T. S. Stein, and W. E. Kauppila, J. Phys. B 14, L783 (1981).
20. J. M. Dale, L. D. Hulett, and S. Pendyala, Surf. Interface Anal. 2, 199 (1980).
21. G. E. Lee-Whiting, Chalk River Report CRT-673.
22. R. E. Kennerly, Phys. Rev. A 21, 1876 (1980).
23. S. Cvejanović and F. H. Read, J. Phys. B 7, 1180 (1974).
24. P. G. Coleman, T. C. Griffith, and G. R. Heyland, Appl. Phys. 5, 223 (1974).
25. S. C. Liang, Can. J. Chem. 33, 279 (1955).
26. T. Edmonds and J. P. Hobson, J. Vac. Sci. Technol. 2, 182 (1965).
27. G. C. Baldwin and M. R. Gaerttner, J. Vac. Sci. Technol. 10, 215 (1973).

28. R. P. McEachran, D. L. Morgan, A. G. Ryman, and A. D. Stauffer, J. Phys. B 10, 663 (1977); Corrigendum, J. Phys. B 11, 951 (1978).

29. Y. K. Ho and P. A. Fraser, J. Phys. B 9, 3213 (1976).

30. L. Spruch and L. Rosenberg, Phys. Rev. 117, 1095 (1960).

31. M. Gailitis, Soviet Phys. JETP 20, 107 (1965).

32. R. J. Drachman, J. Phys. B 5, L30 (1972).

33. H. Aulenkamp, P. Heiss, and E. Wichmann, Z. Phys. 268, 213 (1974).

34. R. J. Drachman, Phys. Rev. 144, 25 (1966).

35. M. Ya. Amusia, N. A. Cherepkov, L. V. Chernysheva, and S. G. Shapiro, J. Phys. B 9, L531 (1976).

36. D. M. Schrader, Phys. Rev. A 20, 918 (1979).

37. H. S. W. Massey and A. H. Moussa, Proc. Phys. Soc. 77, 811 (1961).

38. M. F. Fels and M. H. Mittleman, Phys. Rev. 182, 77 (1969).

39. P. Mandal, A. S. Ghosh, and N. C. Sil, J. Phys. B 8, 2377 (1975).

40. P. Mandal, D. Basu, and A. S. Ghosh, J. Phys. B 9, 2633 (1976).

41. P. Mandal, S. Guha, and N. C. Sil, J. Phys. B 12, 2913 (1979).

42. P. Khan and A. S. Ghosh, Phys. Rev. A 28, 2181 (1983).

43. J. W. Humberston, Can. J. Phys. 60, 591 (1982).